

A Moist Static Energy Budget–Based Analysis of the Sahel Rainfall Response to Uniform Oceanic Warming

SPENCER A. HILL^a

Program in Atmospheric and Oceanic Sciences, Princeton University, Princeton, New Jersey

YI MING AND ISAAC M. HELD

NOAA/Geophysical Fluid Dynamics Laboratory, Princeton, New Jersey

MING ZHAO

NOAA/Geophysical Fluid Dynamics Laboratory, Princeton, New Jersey, and University Corporation for Atmospheric Research, Boulder, Colorado

(Manuscript received 31 October 2016, in final form 6 March 2017)

ABSTRACT


Climate models generate a wide range of precipitation responses to global warming in the African Sahel, but all that use the NOAA Geophysical Fluid Dynamics Laboratory AM2.1 model as their atmospheric component dry the region sharply. This study compares the Sahel's wet season response to uniform 2-K SST warming in AM2.1 using either its default convective parameterization, relaxed Arakawa–Schubert (RAS), or an alternate, the University of Washington (UW) parameterization, using the moist static energy (MSE) budget to diagnose the relevant mechanisms.

UW generates a drier, cooler control Sahel climate than does RAS and a modest rainfall increase with SST warming rather than a sharp decrease. Horizontal advection of dry, low-MSE air from the Sahara Desert—a leading-order term in the control MSE budget with either parameterization—is enhanced with oceanic warming, driven by enhanced meridional MSE and moisture gradients spanning the Sahel. With RAS, this occurs throughout the free troposphere and is balanced by anomalous MSE import through anomalous subsidence, which must be especially large in the midtroposphere where the moist static stability is small. With UW, the strengthening of the meridional MSE gradient is mostly confined to the lower troposphere, due in part to comparatively shallow prevailing convection. This necessitates less subsidence, enabling convective and total precipitation to increase with UW, although both large-scale precipitation and precipitation minus evaporation decrease. This broad set of hydrological and energetic responses persists in simulations with SSTs varied over a wide range.

1. Introduction

The Sahel is the semiarid transitional region between the Sahara Desert and the savannas of West Africa and northern equatorial Africa. The majority of its annual mean precipitation occurs during the northward excursion

of the intertropical convergence zone (ITCZ) in boreal summer, which manifests in the region's west as the West African monsoon (e.g., Nie et al. 2010) and in its east as a northward shift of continental convection [see review by Nicholson (2013)]. Nevertheless, precipitation and many other surface climate markers are to first order zonally symmetric spanning the Sahel's full width.¹

 Denotes content that is immediately available upon publication as open access.

^aCurrent affiliation: Department of Atmospheric and Oceanic Sciences, University of California, Los Angeles, Los Angeles, and Division of Geological and Planetary Sciences, California Institute of Technology, Pasadena, California.

Corresponding author: Spencer Hill, shill@atmos.ucla.edu

¹ Modest zonal asymmetries in precipitation include local maxima in the far west and east (Cook 1997), the latter being common to continental convection zones (Cook 1994; Chou et al. 2001) but further localized by the topography of the Ethiopian highlands.



This article is licensed under a [Creative Commons Attribution 4.0 license](http://creativecommons.org/licenses/by/4.0/) (<http://creativecommons.org/licenses/by/4.0/>).

The Sahelian hydroclimate varies markedly on interannual to millennial time scales. Famously, a severe drought spanned from the late 1960s to the mid-1980s (Tanaka et al. 1975; Nicholson 1985; Gallego et al. 2015). Although the drought was initially ascribed to a local vegetation–surface albedo–precipitation desertification feedback (Charney 1975; Charney et al. 1975), atmospheric general circulation models (AGCMs) run with fixed vegetation and the observed time series of SSTs generally capture the drought and other observed decadal-scale Sahel rainfall variations (Folland et al. 1986; Giannini et al. 2003), leading to the effects of SST patterns becoming the primary research focus [see review by Rodríguez-Fonseca et al. (2015)].²

Climate model end-of-twenty-first century projections of Sahel rainfall range from severe drying to even greater wettening (e.g., Biasutti 2013), a spread that has not improved over the past two generations of the Coupled Model Intercomparison Project (CMIP), CMIP3 and CMIP5 (e.g., Fig. 11 of Rodríguez-Fonseca et al. 2015). GCMs also project widely varying spatial patterns of SST change (e.g., Fig. 12 of Zhao et al. 2009), leading to arguments that this drives the Sahel rainfall spread. But model-dependent responses to imposed SST anomalies (Rodríguez-Fonseca et al. 2015, and references therein) and nonstationary relationships between Sahel rainfall and various SST indices both in models (e.g., Lough 1986; Biasutti et al. 2008; Losada et al. 2012) and observations (Gallego et al. 2015) have led to continuing disagreement regarding the most important ocean basin or SST pattern, with Atlantic (e.g., Zhang and Delworth 2006), Indian (e.g., Lu 2009), and Arctic (Park et al. 2015) SSTs separately posited as being fundamental.

Irrespective of the spatial signature, GCMs consistently project mean ocean surface warming (Collins et al. 2013), and it has been argued that precipitation changes over tropical land in twenty-first-century simulations are largely controlled by mean ocean warming (He et al. 2014; Chadwick 2016). For the Sahel, while arguments appealing to changes in SST spatial patterns (e.g., Giannini et al. 2013) would project no response to mean warming, CMIP3-era AGCMs perturbed with

uniform 2-K SST warming exhibit rainfall responses in the Sahel ranging from modest to severe drying (Held et al. 2005). The severe drying response, in the NOAA Geophysical Fluid Dynamics Laboratory (GFDL) AM2.1 AGCM, drives comparable drying in twenty-first-century simulations in its coupled atmosphere–ocean configuration, CM2.1. The drying in CM2.1 and its CMIP5-era descendant, ESM2M, are among the most severe drying responses of the CMIP3 (Held et al. 2005) and CMIP5 (Biasutti 2013) ensembles, respectively, and have to date defied interpretation in terms of existing theory for tropical circulation responses to SST perturbations, unlike AM2.1's zonal mean circulation (Hill et al. 2015; Hill 2016). The goal of this study, therefore, is to identify the physical mechanisms underlying this drying response in AM2.1, as a first step toward assessing its plausibility as a real-world response to mean ocean warming.

It can be reasonably expected that the convective parameterization shapes Sahelian precipitation in AM2.1 both in its present-day control climate and in its drying response to SST warming. How moist convection is represented fundamentally shapes the tropical circulation in comprehensive (Zhang 1994; Bernstein and Neelin 2016) and idealized (Frierson 2007) GCMs and alters the Sahelian annual cycle of precipitation in global (McCrary et al. 2014) and regional (Marshall et al. 2013; Im et al. 2014; Birch et al. 2014) AGCMs. Conceptually, the convective parameterization (or any other model component) can influence the response to warming through two orthogonal pathways (cf. Mitchell et al. 1987). First, for a given control climate state, how do the convective processes as parameterized respond to the imposed perturbation? For example, suppose that SST warming resulted in reduced tropospheric relative humidity. All else equal, that drying would inhibit convection more so in a parameterization with substantial entrainment of environmental air than in a parameterization with weak entrainment. Second, for a given parameterization of convective processes, how does the regional climate response depend on the control state? For example, the teleconnection mechanisms by which El Niño produces descent anomalies in remote regions differ depending on the existing circulation in those regions (Su and Neelin 2002), and the “rich-get-richer” scaling response of $P - E$ to warming inherently depends on the existing distribution of $P - E$ (Mitchell et al. 1987; Chou and Neelin 2004; Held and Soden 2006).

In this study, we use present-day control and uniform SST perturbation experiments in AM2.1, using either its standard convective parameterization or an alternate, to determine the processes underlying the

² Vegetation feedbacks still figure centrally in interpretations (e.g., Hales et al. 2006) of the onset of the African Humid Period of ~14.8–5.5 ka, wherein abundant rainfall and vegetation spanned the Sahel and most of the Sahara (e.g., Shanahan et al. 2015). Also, interannual variations are typically amplified and agreement with observations improved when vegetation is made dynamic (e.g., Zeng et al. 1999; Giannini et al. 2003). Furthermore, based on AGCM simulations, Dong and Sutton (2015) attribute the observed recovery from drought since the 1980s primarily to direct forcing by increasing greenhouse gases rather than SSTs.

Sahel's hydrological and energetic responses to warming. Following a description of the experimental design and model attributes (section 2), we show that the region's hydroclimate, both in present-day control simulations and in response to SST warming, differs markedly between the two convective parameterizations (section 3). Specifically, the alternate parameterization generates shallower convection, less precipitation, and a cooler surface in the control simulation compared to the default parameterization and modestly increased precipitation in response to SST warming rather than severe drying. The physical mechanisms behind these discrepancies are then diagnosed through the moist static energy (MSE) budget. The two convection schemes yield the same leading-order balance in the region-mean MSE budget in the control simulation (section 4), but fundamentally different MSE responses to SST warming (section 5). By varying SSTs uniformly over a wide range, we better determine the relative roles of the formulation of the convective processes and the large-scale climate (section 6). We conclude with discussion (section 7) and a summary (section 8) of the results.

2. Methodology

AM2.1 (GFDL Global Atmospheric Model Development Team 2004; Delworth et al. 2006) uses a finite-volume, latitude–longitude dynamical core with 2° latitude \times 2.5° longitude horizontal resolution, 24 vertical levels extending to 10 hPa, prescribed monthly aerosol burdens, the LM2 land model (Milly and Shmakin 2002), and the relaxed Arakawa–Schubert (RAS) convective parameterization (Arakawa and Schubert 1974; Moorthi and Suarez 1992). RAS represents moist convection as an ensemble of plumes originating from the boundary layer, each detraining cloudy air only at cloud top and entraining environmental air at all levels at a rate computed inversely based on their buoyancy and specified cloud-top height. The RAS implementation in AM2.1 uses the minimum-entrainment parameter of Tokioka et al. (1988), which prohibits convection that would otherwise have an entrainment rate lower than a specified minimum value that is inversely proportional to the boundary layer depth.

We create a modified version of AM2.1 by replacing RAS with a modified version of the University of Washington (UW) parameterization (Bretherton et al. 2004). UW represents moist convection as a single bulk plume that entrains environmental air and detrains cloudy air at each level as it ascends, with entrainment inversely proportional to convective depth. This scheme has been used in other GFDL models, both in its original intended capacity as a shallow convective

parameterization (AM3; Donner et al. 2011) and as the parameterization for all convection (HiRAM; Zhao et al. 2009; Zhao 2014). We use the same settings for UW as in its implementation in HIRAM, including a reduction in entrainment over land necessary to generate adequate convective continental precipitation. We use a value of 0.5 for this land–ocean entrainment ratio, the same as that used by HIRAM when run at this horizontal resolution; for reference, HIRAM uses a value of 0.75 when run at 50-km resolution and a value of 1.0 at 25-km resolution [see Fig. 1 and corresponding text of Zhao et al. (2009)]. The convective parameterization is the sole difference between the two model variants. UW was chosen as the alternative parameterization based on preliminary results in HIRAM that showed large differences compared to AM2.1 in the rainfall response to SST warming. For the remainder of this paper, we use the acronyms RAS and UW to refer to the respective model variants in addition to the parameterizations themselves.

We perform control and perturbation simulations in both RAS and UW. The control simulation comprises present-day climatological annual cycles of SSTs and sea ice repeated annually, the SSTs computed over 1981–99 from the NOAA Optimal Interpolation dataset (Reynolds et al. 2002). In the perturbation simulation, 2 K is added uniformly to the SSTs. Concentrations of greenhouse gases and aerosols are fixed at present-day values in all simulations in order to isolate the role of SST warming. The simulations span 31 years, with averages taken over the last 30. All values presented are averages over the rainy season of July through September. Region averages are based on land points within 10° – 20° N, 18° W– 40° E, similar to that of Held et al. (2005). Meridional dipoles and associated sharp gradients within the Sahel in many terms complicate the interpretation of region-mean quantities, and we therefore note for region-mean values the extent to which they reflect in-region cancellation.

We use data on the model's native hybrid sigma–pressure coordinates (Simmons and Burridge 1981) postprocessed to a regular latitude–longitude grid, and this horizontal interpolation step is known to generate spurious mass and energy imbalances (despite retaining the native vertical coordinates; cf. Neelin 2007). As such, in appendix A we present an adjustment method based on those of Trenberth (1991) and Peters et al. (2008) that imposes nearly exact closure of the column-integrated budgets of conserved tracers, and in appendix B we detail the computation procedures for all MSE budget terms, including the application of this adjustment method to MSE. The adjusted column MSE budget terms are computed using 3-hourly instantaneous data;

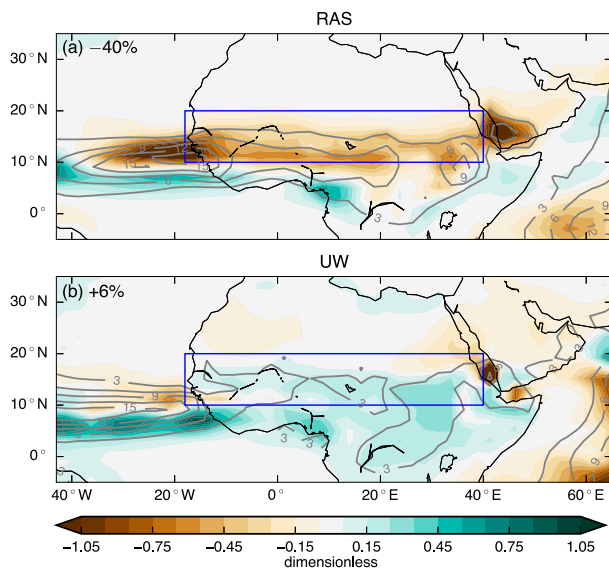


FIG. 1. Difference in precipitation between the uniform 2-K SST warming and present-day control simulations, normalized by the control simulation Sahel region-mean value and therefore unitless (shaded contours), and precipitation in the control simulation, with contours starting at 3 mm day^{-1} and with a 3 mm day^{-1} interval (gray contours), in (a) RAS and (b) UW. In this and subsequent figures, latitude tick marks span from the equator to 30°N in 10° increments, longitude tick marks span from 40°W to 60°E in 20° increments, blue boxes delineate the boundaries used to compute Sahel region-mean values, and values printed in the top left of each panel are the Sahel region-mean values of the field in shaded contours (in this case the precipitation response).

other fields are computed from time series of monthly averages.

3. Precipitation and surface climate

Figure 1 shows precipitation in the control simulations as gray contours, and Table 1 lists Sahel region-mean values of precipitation, surface temperature, and other surface climate fields. The Sahel region-mean precipitation is 4.0 mm day^{-1} in RAS and 2.6 mm day^{-1} in UW, a large discrepancy that mostly reflects lower precipitation rates in UW in the southern Sahel. This comparative dryness in UW occurs over most land (not shown), as the UW parameterization is less effective than RAS at generating continental convection. Region-mean values of evaporation (E) are more similar than precipitation (P) in the control simulation (2.3 and 2.4 mm day^{-1} for evaporation in RAS and UW, respectively; Table 1). As a result, precipitation minus evaporation ($P - E$) is 1.7 mm day^{-1} in RAS but only 0.3 mm day^{-1} in UW in the control simulation, near the lower limit for a land region of zero (since subground horizontal moisture transport is negligible on spatial scales larger than individual catchments, evaporation

TABLE 1. Sahel region-mean values of, from left to right: total precipitation, precipitation from the convective parameterization, precipitation from the large-scale condensation scheme, evaporation, precipitation minus evaporation (all mm day^{-1}), surface air temperature (K), and relative humidity 2 m above the surface (percent) for the control simulation, 2-K SST warming simulation, and their difference, in both model variants.

Model	Run	\bar{P}	\bar{P}_{conv}	\bar{P}_{ls}	\bar{E}	$\bar{P} - \bar{E}$	\bar{T}_s	$\text{RH}_{2\text{m}}$
RAS	Control	4.0	3.7	0.2	2.3	1.7	300.9	64
	+2 K	2.3	2.2	0.1	1.9	0.4	305.5	52
	difference	-1.7	-1.5	-0.1	-0.4	-1.3	+4.6	-12
UW	Control	2.6	1.9	0.7	2.4	0.3	299.5	59
	+2 K	2.8	2.4	0.5	2.6	0.2	302.2	56
	difference	+0.2	+0.4	-0.2	+0.2	-0.1	+2.7	-3

cannot exceed precipitation on climatic time scales). Near-surface relative humidity is also lower in UW (Table 1); by all of these measures the control Sahelian climate is more arid in UW than in RAS. Precipitation compares more favorably with observations in RAS than in UW (not shown); however, fidelity to observations in control simulations within the region is known to be a poor predictor of a GCM's precipitation response in twenty-first-century simulations (Cook and Vizi 2006).

The precipitation responses to 2-K SST warming in RAS and UW are shown in Fig. 1, normalized by the Sahel region-mean precipitation in their respective control simulations. As documented by Held et al. (2005), rainfall decreases sharply over most of the Sahel in RAS, by 40% (1.7 mm day^{-1}) in the region average. This is part of a larger spatially coherent drying, with even greater precipitation decreases just to the east (over the southern Arabian Peninsula and Red Sea) and west (over the Atlantic Ocean). For context, precipitation reductions in excess of 4 mm day^{-1} occur in several grid points within this band and nowhere else globally. Also, $P - E$ declines sharply (by 1.3 mm day^{-1}). In sharp contrast, precipitation *increases* modestly over most of the Sahel in UW, by 6% (0.2 mm day^{-1}) on average, although a slightly larger increase in evaporation causes $P - E$ to decrease.

The total precipitation in each grid cell of a GCM is the sum of the precipitation generated by the convective parameterization and by the large-scale cloud parameterization, and Table 1 lists the precipitation originating from each for each simulation. In RAS compared to UW, less of the precipitation is generated by the large-scale parameterization, in both absolute and fractional terms (Table 1). With 2-K SST warming, in RAS both precipitation types decrease, whereas in UW convective precipitation increases by 0.4 mm day^{-1} while large-scale precipitation decreases by 0.2 mm day^{-1} . We

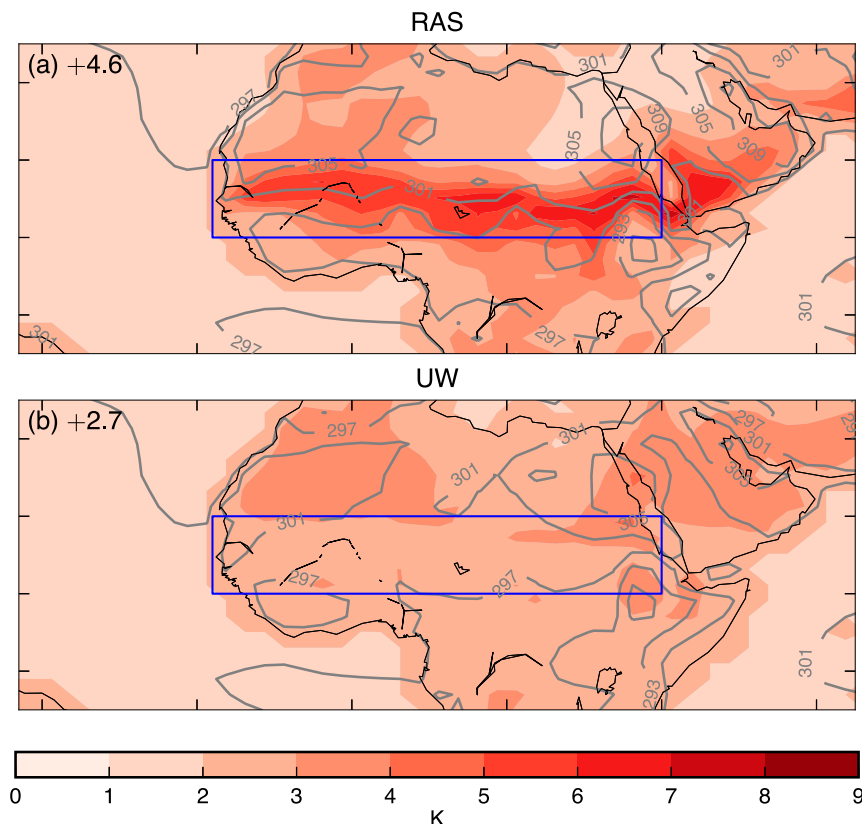


FIG. 2. As in Fig. 1, but for surface air temperature. Difference in surface air temperature between the uniform 2-K SST warming and present-day control simulations (in K; shaded contours), and surface air temperature in the control simulation, with contours values printed (in K; gray contours), in (a) RAS and (b) UW.

return to the disparate responses to SST warming in UW between convective and large-scale precipitation and between precipitation and $P - E$ in section 6.

Figure 2 shows surface air temperature in the control simulation and the responses to 2-K SST warming. The Sahel is 1.5 K warmer in the control simulation in RAS than in UW, which reflects greater low cloud cover in UW (not shown). SST warming generates land-amplified surface air warming in both model variants, but in RAS the Sahel warming is a global maximum: warming exceeds 6 K over much of the Sahel, with a maximum of 9.0 K in the eastern Sahel, and does not exceed 6 K anywhere outside the region (not shown). In UW, Sahel surface warming is unexceptional, with a region mean of 2.7 K. Near-surface relative humidity decreases sharply in RAS, from 64% to 52%, and more modestly in UW, from 59% to 56%.

Given the precipitation responses in each model variant, the corresponding surface temperature and relative humidity responses are consistent with theoretical expectations. Under global warming, surface warming is land amplified in both transient and equilibrium

contexts (Byrne and O’Gorman 2013a,b). Combined with modest global mean and ocean-mean relative humidity change, this land-amplified warming causes relative humidity over land to decrease. Largely as a result, terrestrial aridity (defined, e.g., as the ratio of precipitation to potential evapotranspiration) generally increases at low and middle latitudes (Scheff and Frierson 2014; Sherwood and Fu 2014; Scheff and Frierson 2015). As such, in global warming simulations changes to precipitation and surface temperature over tropical land are anticorrelated (Chadwick 2016), and most of the land regions that warm more than the global land average are semiarid regions in which precipitation has decreased (Berg et al. 2015).

4. Moist static energy budget in the control simulations

a. Existing theory

The column-integrated MSE budget succinctly encapsulates the character of tropical circulations and is

ubiquitous in investigations of how those circulations respond to climatic perturbations. Denoting MSE by h , then $h \equiv c_p T + gz + L_v q_v - L_f q_i$, where c_p is the specific heat of air at constant pressure, T is temperature, g is the gravitational constant, z is geopotential height, L_v is the latent heat of vaporization of water, q_v is specific humidity, L_f is the latent heat of fusion of water, and q_i is specific mass of ice. MSE therefore comprises potential energy and sensible and latent enthalpy while neglecting kinetic energy. Denoting column-mass integrals with curly brackets ($\{\cdot\} \equiv \int_0^{p_s} (dp/g)$, where p_s is surface pressure), time averages with overbars, and deviations from the time-average with primes, the time mean, column-integrated MSE budget may be expressed as

$$\frac{\partial}{\partial t} \{\overline{\mathcal{E}}\} + \{\overline{\mathbf{v}} \cdot \nabla_p \overline{h}\} + \left\{ \overline{\omega} \frac{\partial \overline{h}}{\partial p} \right\} + \nabla \cdot \{\overline{h' \mathbf{v}'}\} \approx \overline{F}_{\text{net}}, \quad (1)$$

where $\mathcal{E} \equiv c_v T + gz + L_v q_v - L_f q_i$ is internal plus potential energy, c_v is the specific heat of air at constant volume, \mathbf{v} is horizontal velocity, ∇_p is the horizontal divergence operator at constant pressure, and F_{net} is the net energetic forcing. F_{net} comprises top-of-atmosphere (TOA) and surface radiative fluxes (R_t and R_s , respectively) and surface turbulent fluxes of sensible (H) and latent enthalpy ($L_v E$, where E is evaporation; all signed positive directed into the atmosphere):

$$F_{\text{net}} \equiv L_v E + H + R_t + R_s. \quad (2)$$

Notably, convective diabatic moistening and heating terms that appear (often with large magnitude) at individual levels must cancel in the column integral, one of the key draws of (1). For land, the small heat capacity renders the net surface energy flux zero on climatic time scales, and therefore the net energetic forcing $\overline{F}_{\text{net}}$ reduces to the top-of-atmosphere radiative flux \overline{R}_t . Conceptually, energetic input into the atmospheric column through its upper and lower boundaries must be balanced by some combination of column-integrated time-mean horizontal MSE advection ($\{\overline{\mathbf{v}} \cdot \nabla_p \overline{h}\}$, typically dominated by the large-scale rotational flow), column-integrated time-mean vertical MSE advection ($\{\overline{\omega} \partial_p \overline{h}\}$, inherently due to the divergent flow), and column-integrated transient eddy MSE flux divergence ($\nabla \cdot \{\overline{h' \mathbf{v}'}\}$), less any change in column-integrated total internal energy ($\partial_t \{\overline{\mathcal{E}}\}$). See Hill (2016) and references therein for discussion of the approximations implicit in (1).

The classical picture of a tropical convecting region comprises positive energetic forcing balanced by the time-mean divergent circulation, $\overline{F}_{\text{net}} \approx \{\overline{\omega} \partial_p \overline{h}\}$: convergence of mass and MSE in the boundary layer, deeply penetrating moist convection, and convective outflow

near the tropopause diverging mass and more MSE than is converged in the boundary layer (Neelin and Held 1987). However, the first baroclinic MSE profile typical of the tropics (minimum in the midtroposphere) renders the MSE export by the divergent circulation sensitive to the depth of the convection—if sufficiently shallow, the divergent circulation actually imports MSE in the column integral. On the time scale of a convective life cycle, this transport of moisture and MSE into the free troposphere by shallow convection conditions the column for subsequent deep convection (e.g., Wu 2003; Inoue and Back 2015). On climatic time scales, this must be balanced by MSE export through some combination of transient eddies and the time-mean horizontal flow (e.g., Back and Bretherton 2006; Bretherton et al. 2006).

b. Results

1) RAS

Figure 3 shows the column-integrated MSE budget terms in the control simulations. In all panels, red shades signify import of MSE (i.e., positive $\overline{F}_{\text{net}}$ values and negative transport term values) and blue shades signify export of MSE (i.e., negative $\overline{F}_{\text{net}}$ values and positive transport term values). In and near the Sahel, the MSE budget varies markedly with latitude. The southern Sahel and equatorial Africa conform to the classical picture of tropical convecting regions: large energetic forcing ($\sim 100 \text{ W m}^{-2}$; Fig. 3a) balanced primarily by MSE export by the time-mean divergent circulation (Fig. 3e).³ Moving northward, while the energetic source term remains mostly positive within the Sahel, the divergent circulation term becomes steadily more negative, yielding net MSE import over most of the northern Sahel ($\sim 70 \text{ W m}^{-2}$), where presumably much of the convection is dry. The combined positive energetic inputs by the forcing and divergent circulation in the northern Sahel are balanced by large magnitude export of MSE by the time-mean horizontal flow ($\sim 100 \text{ W m}^{-2}$; Fig. 3c).

Figure 4 shows MSE and horizontal wind at two model levels, in the boundary layer and midtroposphere, respectively. In RAS, boundary layer MSE (Fig. 4a) in the southern Sahel and equatorial Africa is high and fairly homogeneous, a structure that fuels deep convection while curtailing horizontal MSE advection (Sobel 2007). The meridional MSE gradient is sharp in the northern Sahel, which is dominated by the meridional moisture gradient (the temperature gradient

³ Large horizontal and vertical advection values in the far southeastern Sahel stem from the topography of the Ethiopian highlands.

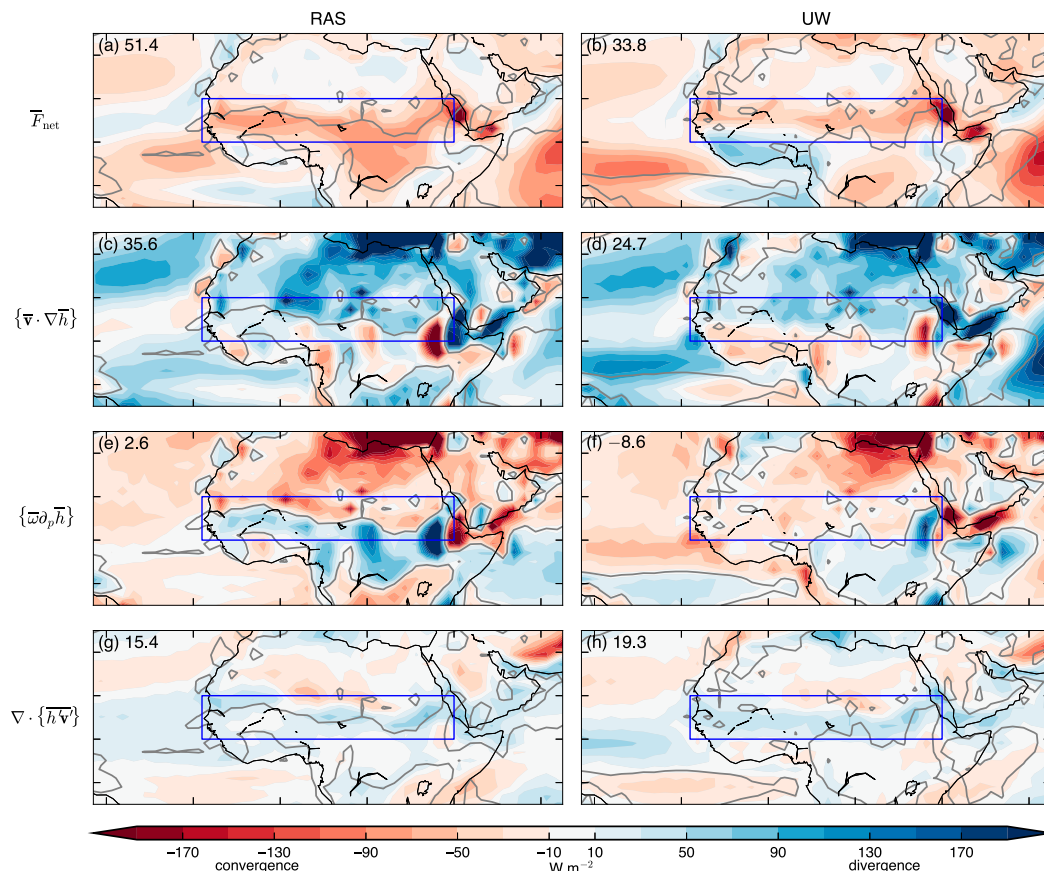


FIG. 3. Terms of the control simulation column-integrated MSE budget in (left) RAS and (right) UW (in W m^{-2} ; shaded contours): from top to bottom, net energetic forcing, time-mean horizontal advection, time-mean vertical advection, and eddy flux divergence. The color bar corresponds to the three transport terms, for which red shades denote import (negative values), and blue shades export (positive values), of MSE. For the net energetic forcing term, the sign is opposite to the color bar, with red (blue) shades denoting positive (negative) net energetic forcing values. With these conventions, for all terms red shades can be thought of as representing a gain, and blue shades a loss, of energy. The gray contour in all panels is the zero contour of the time-mean vertical advection. The storage term ($\partial_t \bar{\epsilon}$) is omitted. It is the smallest magnitude term and does not factor into the response appreciably. Values in the top-left corner of each panel are the Sahel region-mean values, in W m^{-2} .

slightly counteracts this), and this is acted on by northerly winds to yield strong MSE export. In the mid-troposphere (Fig. 4c), horizontal MSE gradients are weaker and the flow is more zonal and uniform than in the boundary layer, leading to little net horizontal MSE advection at this level. Consequently, the column-integrated horizontal MSE advection is dominated by the lower troposphere—as indicated by Fig. 5, which shows the Sahel region-mean vertical profiles of the net energetic forcing and time-mean horizontal and vertical advection terms—and by meridional (rather than zonal) advection (not shown).

Largely opposing the time-mean horizontal circulation, the time-mean divergent flow (Fig. 5c) imports MSE at lower levels and exports it above. Figure 6 shows the region-mean profiles of vertical velocity and moist

static stability. Ascent occurs throughout the troposphere and acts on negative values of moist static stability above, and positive values below, ~ 700 hPa, consistent with Fig. 5c.

Table 2 lists the Sahel region-mean column-integrated MSE budget terms. Because of the meridional cancellation of the time-mean vertical advection term, the leading-order balance is of net energetic forcing (51.4 W m^{-2}) balanced by export of MSE by the time-mean horizontal circulation (35.6 W m^{-2}). Time-mean vertical advection contributes only 2.6 W m^{-2} and transient eddies a nonnegligible 15.4 W m^{-2} . The meridional dipole of the transient eddy MSE flux divergence (Fig. 3g) presumably reflects northward moisture transport by African easterly waves, which track the sharp meridional gradient in soil moisture that spans the

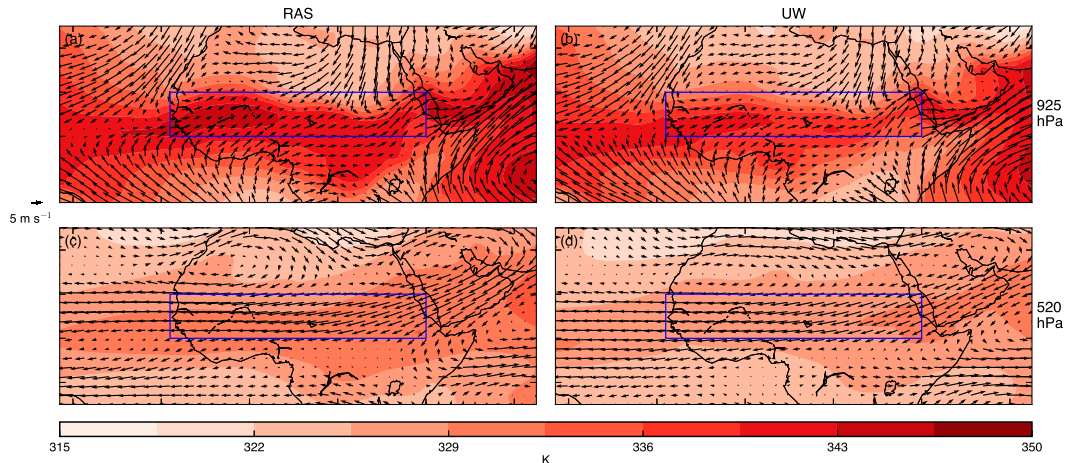


FIG. 4. MSE in the control simulation, divided by c_p such that units are K (shaded contours), and horizontal wind, in m s^{-1} (arrows) at the model levels corresponding roughly to (top) 925 hPa and (bottom) 520 hPa, in (left) RAS and (right) UW.

width of the Sahel (e.g., [Thorncroft et al. 2008](#), and references therein). The budget residual is a negligible 0.3 W m^{-2} , reflecting the adjustment applied to impose near-exact closure. The overall meridional structure within the region of each MSE budget term and of precipitation is slightly tilted, northwest to southeast. This likely reflects the wettening effect of the West African monsoon in the western Sahel, although there is also a zonal component with westerly onshore flow spanning the Sahel's western edge.

2) UW

In UW, the column-integrated net energetic forcing ([Fig. 3b](#)) spatial structure is similar to that of RAS, but within the Sahel values are generally smaller; the region mean is 33.8 W m^{-2} . This arises from the cooler surface and more extensive low cloud cover in UW, which respectively yield less net emission of longwave radiation and less absorption of shortwave radiation (not shown). Export of MSE by horizontal advection spans most of the Sahel ([Fig. 3d](#)), 24.7 W m^{-2} on average, yielding the same leading order region-mean balance as in RAS, $\bar{F}_{\text{net}} \approx \{\bar{\mathbf{v}} \cdot \nabla h\}$. The horizontal flow is largely similar in both the boundary layer and mid-troposphere to RAS ([Figs. 4b and 4d](#), respectively), but MSE values and their meridional gradient at both levels are weaker in UW than in RAS. Modest MSE import in the midtroposphere in UW arises from easterly wind acting on a modest zonal MSE gradient in the eastern Sahel.

Unlike RAS, convection is sufficiently shallow that vertical advection imports MSE in the column integral throughout nearly the entire Sahel ([Fig. 3f](#)), 8.6 W m^{-2} in the region mean. This discrepancy primarily stems

from much weaker upper-tropospheric ascent in UW ([Fig. 6](#)), an intuitive result in a convecting region given that UW is a less active parameterization than RAS. Also, contrary to classical expectation, vertical MSE advection does not track the near surface MSE maximum: the former is positive only within equatorial Africa, in which (unlike RAS) MSE values are low. The eddy flux divergence ([Fig. 3h](#)) resembles that of RAS, with a region-mean value of 19.3 W m^{-2} export. The region-mean profiles of the net energetic forcing and time-mean advection terms ([Figs. 5d–f](#)) are each qualitatively similar to their RAS counterparts, with vertical advection in UW reflecting shallower convection and associated overturning circulation.

5. Moist static energy budget responses to SST warming

In this section, we argue that the changes in the MSE budget that distinguish RAS from UW most importantly are in the midtroposphere. The dominant change at these levels in RAS is increased MSE loss due to horizontal advection, driven primarily by the enhancement of the prevailing meridional MSE gradient ([Boos and Hurley 2013](#)). This is balanced by anomalous midtropospheric subsidence and the resulting adiabatic warming, with little net energetic forcing response. Both the thermodynamic increase in the cooling due to horizontal advection and the dynamic increase in subsidence warming are smaller in UW. Of direct relevance to this behavior is the “upped ante” mechanism ([Neelin et al. 2003](#); [Chou and Neelin 2004](#)), wherein under global warming precipitation on convective margins is suppressed

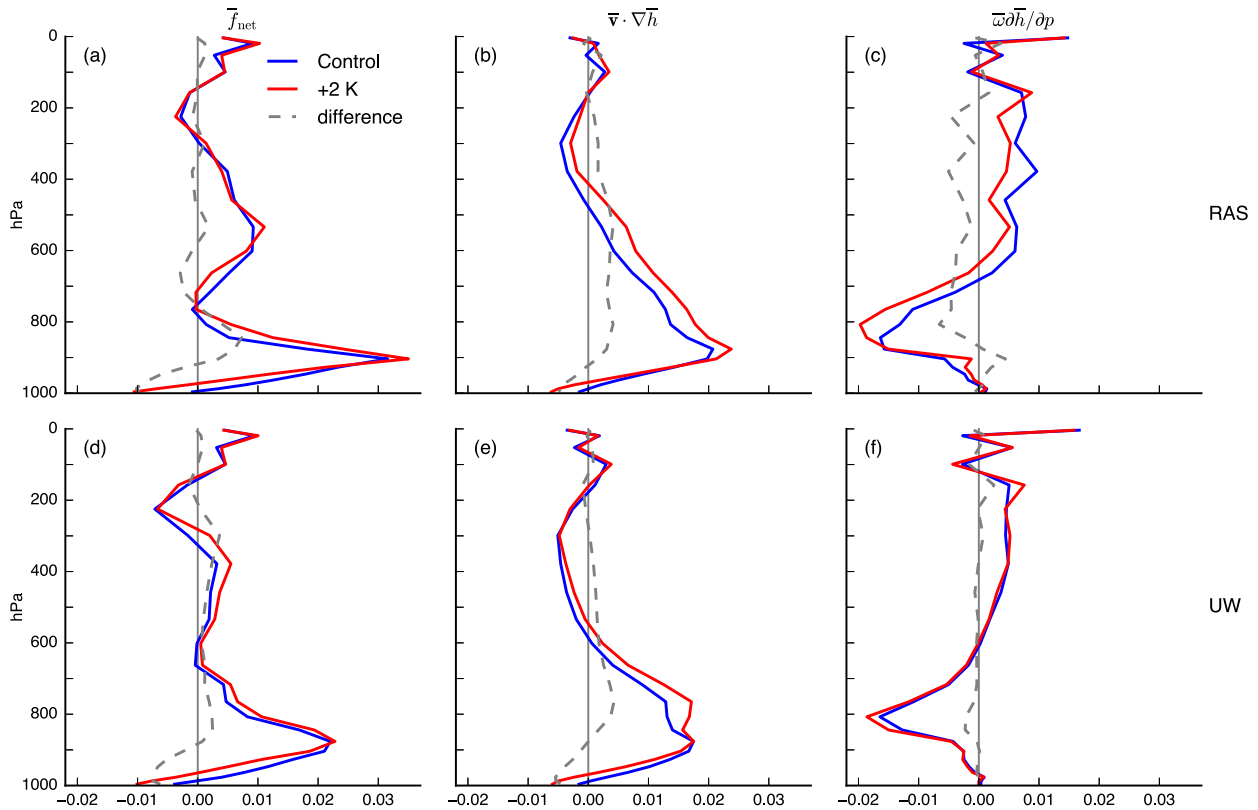


FIG. 5. Sahel region-mean profiles of (left) the net energetic forcing term, (middle) time-mean horizontal MSE advection, and (right) time-mean vertical MSE advection, for the control simulation (blue curve), the 2-K SST warming simulation (red curve), and their difference (dashed gray curve), in (top) RAS and (bottom) UW, in $\text{J kg}^{-1} \text{s}^{-1}$. The two advection terms are signed such that positive values denote export of MSE. The advection terms are computed using monthly data with no column adjustment applied. Vertical advection is computed explicitly using model outputted $\bar{\omega}$ and \bar{h} rather than as a residual.

by inflow acting on enhanced prevailing moisture gradients.

a. RAS

Figure 7 shows the responses of each column-integrated MSE budget term to the +2-K SST perturbation, and Table 2 lists the Sahel region-mean responses and +2-K simulation values. In RAS, the largest responses are of the time-mean advection terms and occur primarily near and just north of the climatological $\{\bar{\omega} \partial_p \bar{h}\} = 0$ isoline that roughly bisects the Sahel. Specifically, MSE export by horizontal advection is strongly enhanced (Fig. 7c; region mean $+20.0 \text{ W m}^{-2}$), balanced by anomalous MSE import by the time-mean divergent circulation (Fig. 7e; region mean -15.9 W m^{-2}). Based on the region-mean profiles of the anomalous advection terms shown in Fig. 5, these column-integrated responses reflect consistent behavior throughout the free troposphere for both terms. The net energetic forcing (Fig. 7a; region mean $+0.9 \text{ W m}^{-2}$) and eddy flux divergence (Fig. 7g; region mean -2.8 W m^{-2}) responses are comparatively modest, comprising moderate

magnitudes oriented in a meridional dipole that largely cancel in the region mean. For eddies, this is primarily in the eastern Sahel and reflects the aforementioned local southward shifts of the temperature and moisture gradients. The anomalous time-mean vertical advection also exhibits a meridional dipole, despite its large region-mean value, and its location relative to the climatological zero line reflects a southward shift of the latter.

We next investigate the mechanisms that give rise to the leading-order balance between the anomalous time-mean advection terms. In addition to the control simulation values already discussed, Fig. 6 also includes region-mean profiles of the vertical velocity and moist static stability in the 2-K warming simulation and the differences with the control simulation. Ascent is drastically reduced throughout the free troposphere and slightly enhanced in the boundary layer, which amounts to a severe shallowing of convection. This dominates over modest moist static stability responses, which we show by decomposing the horizontal and vertical MSE advection responses into dynamic, thermodynamic, and

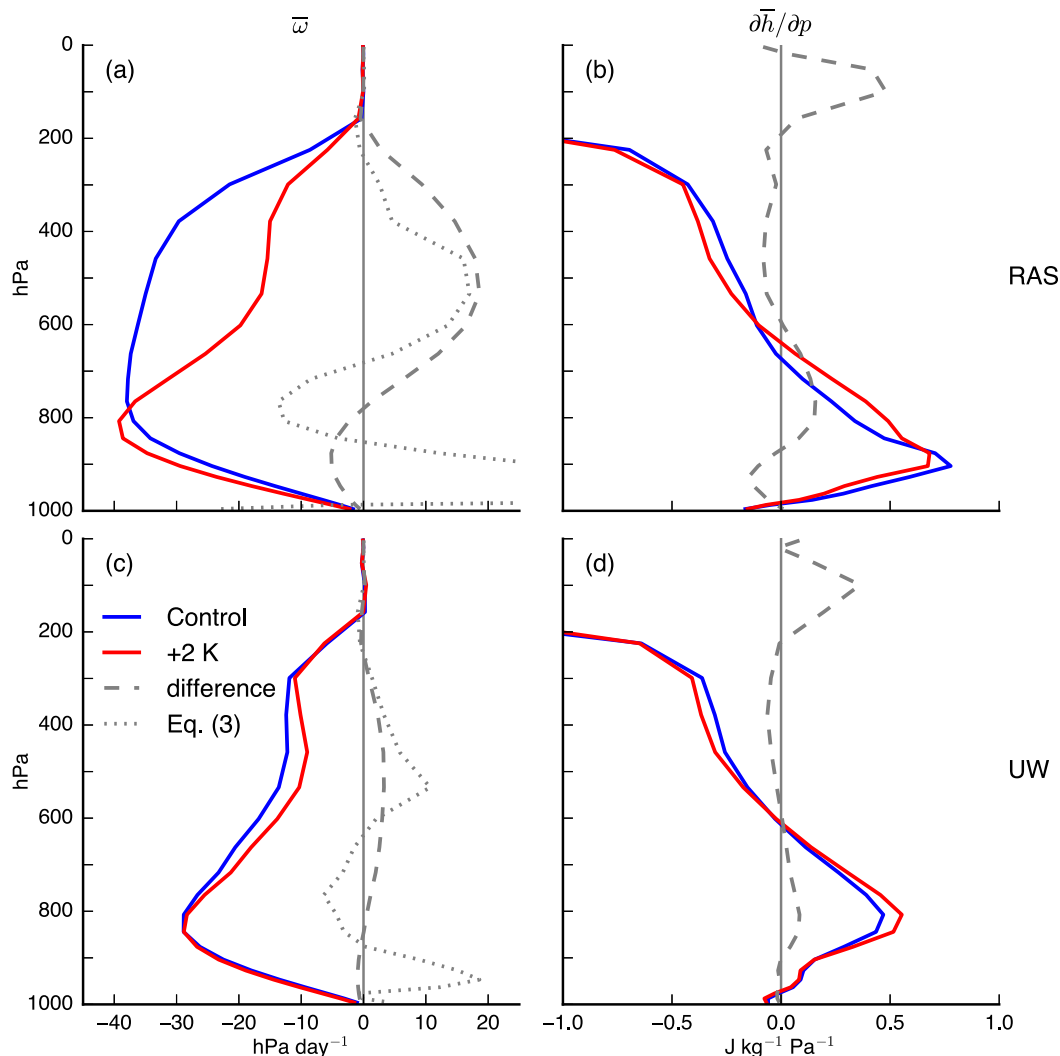


FIG. 6. Sahel region-mean profiles of (left) vertical velocity, in hPa day^{-1} , and (right) moist static stability, in $\text{J kg}^{-1} \text{Pa}^{-1}$, for the control simulation (blue curve), the 2-K SST warming simulation (red curve), and their difference (dashed gray curve), in (top) RAS and (bottom) UW. The dotted gray curve in (a) and (c) is the approximation for $\bar{\omega}$ given by (3), computed at each grid point and month excluding where $|\partial_p \bar{h}| < 0.05 \text{ J kg}^{-1} \text{Pa}^{-1}$ before temporally and regionally averaging. Positive values of $\bar{\omega}$ signify descent, and positive values of $\partial \bar{h} / \partial p$ signify that MSE is increasing with pressure, i.e., decreasing with height. Thus signed, the vertical advection term is exporting MSE when $\bar{\omega}$ and $\partial \bar{h} / \partial p$ are of the same sign.

covarying components that arise respectively from the anomalous flow, from the anomalous MSE, and from the covariance of these two anomaly fields [i.e., for vertical advection, $\delta(\omega \partial_p h) = (\delta \omega) \partial_p h + \omega (\delta \partial_p h) + (\delta \omega)(\delta \partial_p h)$]. The thermodynamic term includes the full response of MSE (i.e., it does not assume fixed-relative humidity). The Sahel region-mean profiles of these terms are shown in Fig. 8 and column-integrated values in Fig. 9. For vertical advection, the dynamic term is dominant throughout the free troposphere and in the column integral. In the northern Sahel, the combination of moderate anomalous ascent in the boundary layer, anomalous

descent in the free troposphere, and reduced relative humidity and precipitation suggest increased dry convection. In the southwestern Sahel, MSE export through vertical advection actually increases, despite precipitation decreasing sharply (Fig. 1a).

The time-mean horizontal MSE advection response in RAS primarily reflects the drying influence of an increased meridional MSE gradient spanning the Sahel. Figure 10 shows the responses of MSE and horizontal wind at the same midtropospheric and boundary layer levels shown in Fig. 4. At both levels, MSE increases more in equatorial Africa than surrounding regions, including

TABLE 2. Terms of the Sahel region-mean column-integrated MSE budget, in W m^{-2} , for the control simulation, 2-K SST warming simulation, and their difference, in both model variants.

Model	Simulation	\bar{F}_{net}	$\{\bar{\mathbf{v}} \cdot \nabla \bar{h}\}$	$\left\{\bar{\omega} \frac{\partial \bar{h}}{\partial p}\right\}$	$\nabla \cdot \{\bar{h}' \mathbf{v}'\}$	$\frac{\partial \{\mathcal{E}\}}{\partial t}$
RAS	Control	51.4	35.6	2.6	15.4	-1.9
	2 K	52.3	55.5	-13.2	12.6	-2.4
	2 K - Control	+0.9	+20.0	-15.9	-2.8	-0.4
UW	Control	33.8	24.7	-8.6	19.3	-1.5
	2 K	37.7	31.9	-11.1	18.4	-1.4
	2 K - Control	+3.9	+7.2	-2.4	-0.9	+0.0

the Sahel and the Sahara Desert. This anomalous gradient predominantly reflects differential increases in water vapor that arise from mean warming. Figure 11 shows the control and response values in both model variants of the column-integrated water vapor throughout the tropics. As expected, relative humidity variations on a tropics-wide scale are modest (not shown), and thus column water vapor increases almost everywhere and generally more in regions where it is climatologically large.

The thermodynamic term dominates the region-mean anomalous MSE export in the free troposphere (Fig. 8a) and yields column-integrated MSE export over most of the Sahel except the far west and east (Fig. 9a)—we return to the boundary layer and northeastern Sahel responses further below. Combined with the dominance of the dynamic component of vertical advection in the free troposphere (Fig. 8b) and a modest net energetic forcing term response above ~ 700 hPa (Fig. 5b), the leading-order balance at these levels is $\bar{\mathbf{v}} \cdot \delta \nabla \bar{h} \approx (\delta \bar{\omega}) \partial_p \bar{h}$. Rearranging this yields an approximate diagnostic for the anomalous ascent profile in the free troposphere:

$$\delta \bar{\omega} \approx -\frac{\bar{\mathbf{v}} \cdot \delta \nabla \bar{h}}{\partial_p \bar{h}}. \quad (3)$$

Figure 6a shows the anomalous vertical motion predicted by (3) for RAS. To avoid unphysical values near where the denominator vanishes, we exclude locations and months where $|\partial_p \bar{h}| < 0.05 \text{ J kg}^{-1} \text{ Pa}^{-1}$ before temporally and regionally averaging; the value of 0.05 was

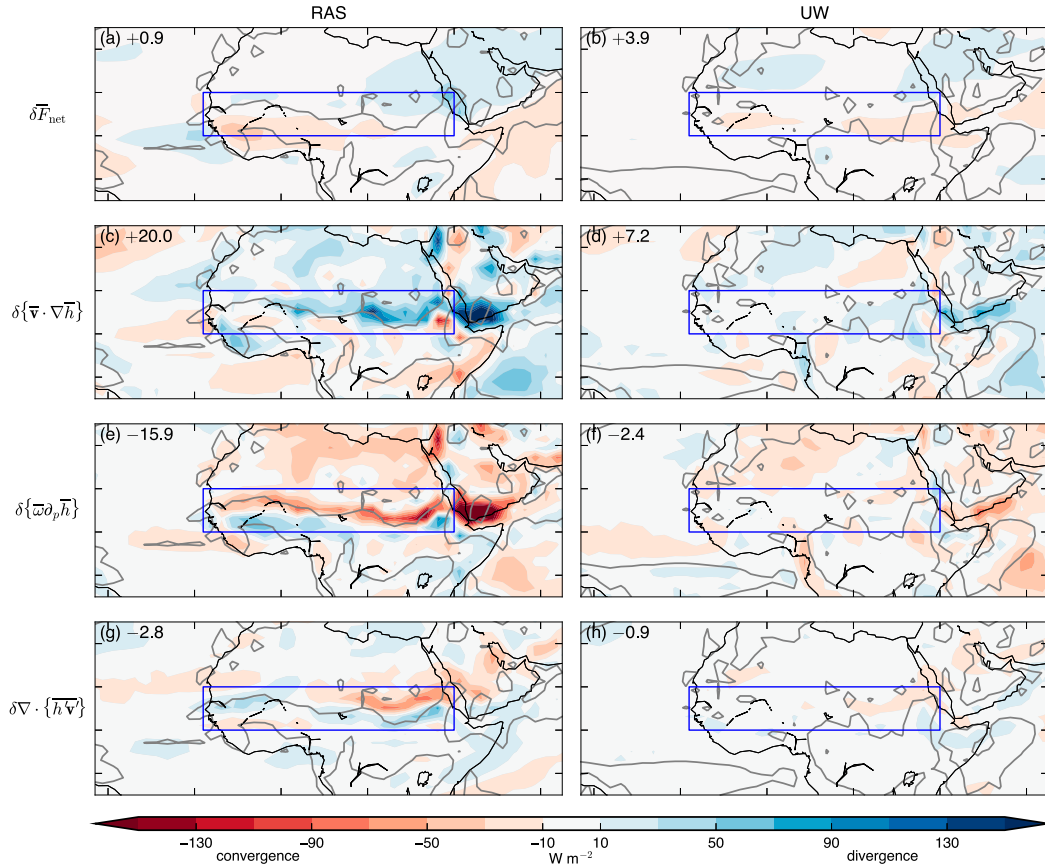


FIG. 7. As in Fig. 3, but with shaded contours denoting the +2-K minus control values. Note that the contour spacing is slightly smaller than in Fig. 3. Similar to Fig. 3, for all panels red shades can be thought of as representing anomalous import, and blue shades anomalous export, of energy.

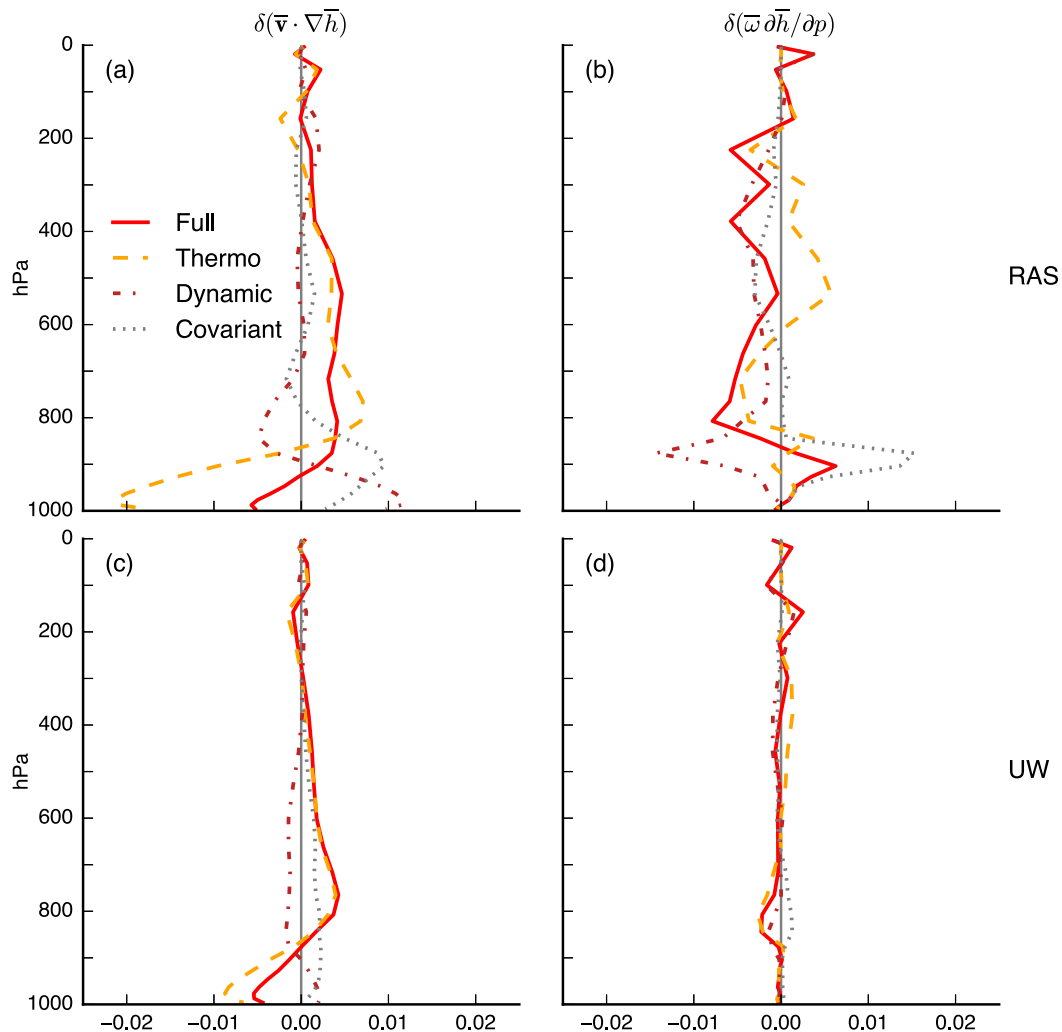


FIG. 8. Profiles of Sahel region-mean values of the 2-K SST warming full response (red curves), and its decomposition into thermodynamic (dashed yellow curves), dynamic (dash-dotted brown curves), and covarying (dotted gray curves) components, for (left) horizontal advection and (right) vertical advection, in (top) RAS and (bottom) UW, in $\text{J kg}^{-1} \text{s}^{-1}$. Sign conventions are the same as for the transport terms in Fig. 5, namely, with positive values signifying export of MSE.

chosen subjectively to provide the best fit. The approximation captures the overall free tropospheric behavior, including the anomalous descent peak in the mid-troposphere. Throughout the free troposphere, the horizontal advection anomaly is positive [$\delta(\bar{\mathbf{v}} \cdot \nabla \bar{h}) > 0$; Fig. 8a] and the moist static stability is negative ($\partial_p \bar{h} < 0$; Fig. 6b). Therefore, anomalous descent ($\delta \bar{\omega} > 0$) is required for the budget to balance. In the midtroposphere, the moist static stability approaches zero, and as such balancing the increased dry advection requires especially large anomalous descent. Suppressed convective precipitation is the straightforward hydrological consequence of this anomalous subsidence.

We now return to the horizontal MSE advection response in the boundary layer, which is dominated by the

response in the northeastern Sahel. Clausius–Clapeyron scaling cannot account for the decreases in column-integrated water vapor in RAS in this region—the only region worldwide where column water vapor decreases (Fig. 11a). This is coincident with large magnitudes in the covarying term of the horizontal advection response (Fig. 9e) and anomalous MSE import from the thermodynamic component (Fig. 9a). In short, these large covariance values reflect a runaway drying and warming response: local surface warming (Fig. 2a) caused by precipitation loss creates an anomalous heat low circulation (Fig. 10a), whose boundary layer inflow is primarily northerly and thus imports even more dry Saharan air, amplifying the drying signal (the compensating mid-tropospheric anticyclonic outflow can be seen in Fig. 10c).

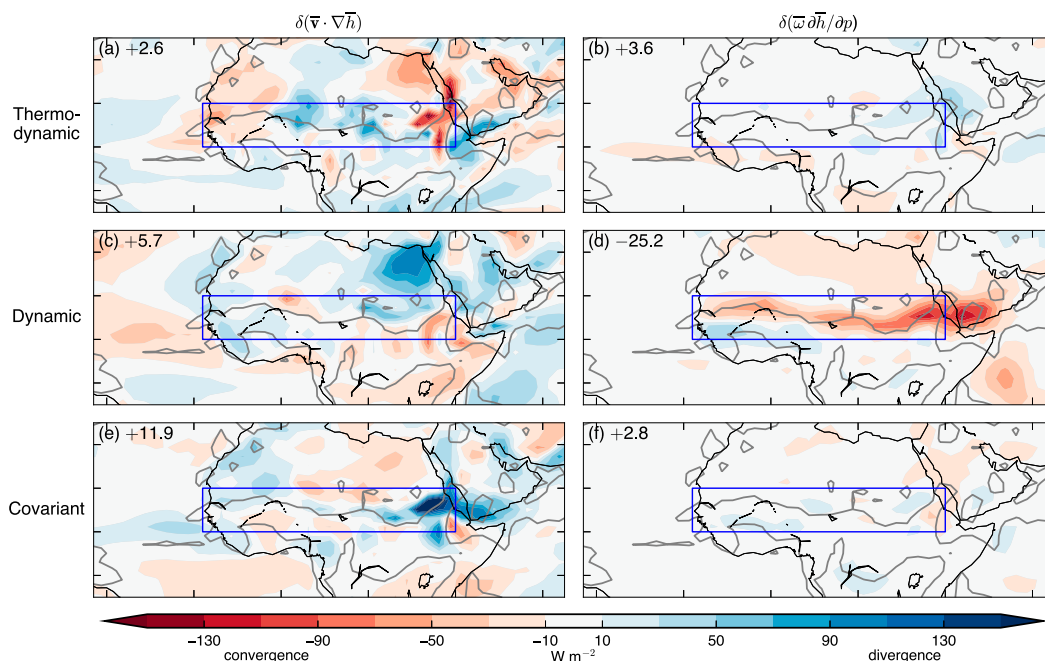


FIG. 9. Decomposition of the (left) horizontal and (right) vertical advection responses in the 2-K SST warming simulation (shaded contours) into (top) thermodynamic, (middle) dynamic, and (bottom) covarying components. All panels are for RAS. Gray contour is the same as in Fig. 3. For expediency, these computations are performed using monthly time series without the column budget adjustment, as detailed in appendix B. As in Fig. 7, for all panels red shades can be thought of as representing anomalous import, and blue shades anomalous export, of energy.

The thermodynamic term behavior locally reflects climatological boundary layer flow from the southwest (Fig. 4a) acting on the anomalous MSE gradient. Combining the thermodynamic and covarying components locally, the increased meridional MSE gradient ultimately drives the drying as in the rest of the northern Sahel.

In summary, increases in water vapor that roughly scale with their climatological values creates an anomalous MSE gradient spanning from equatorial Africa to the Sahara Desert, which, acted on by climatological northerly wind, dries out the Sahel. This inhibits moist convection and its attendant precipitation, and the resulting convective shallowing generates anomalous

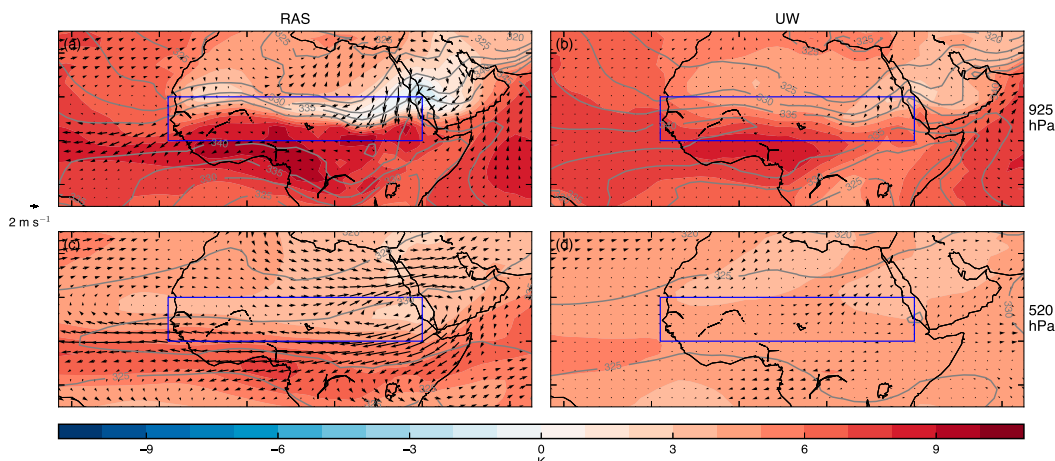


FIG. 10. As in Fig. 4, but for the response in the 2-K SST warming simulation. Responses to 2-K SST warming of MSE, divided by c_p such that units are K (shaded contours), and horizontal wind, in m s^{-1} (arrows), at the model levels corresponding roughly to (top) 925 and (bottom) 520 hPa, in (left) RAS and (right) UW. Note the difference in wind scale compared to Fig. 4.

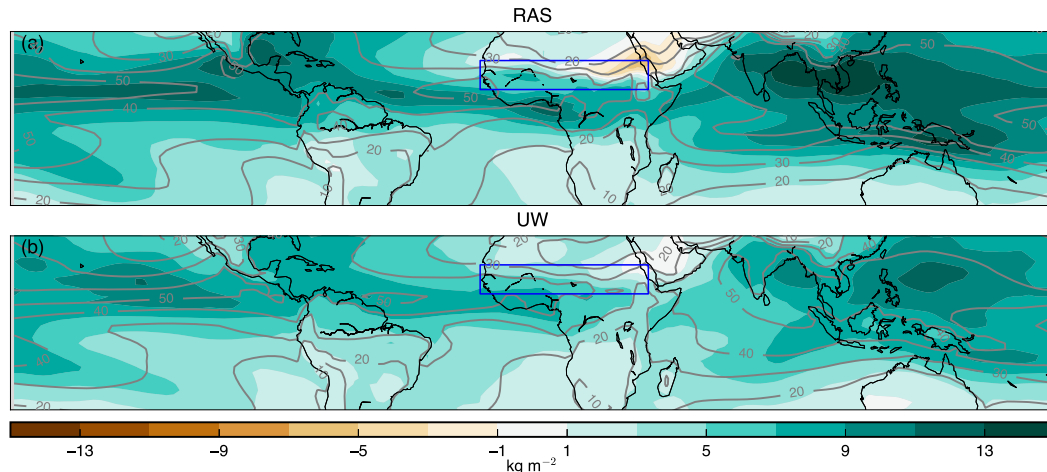


FIG. 11. July–September column-integrated water vapor, in kg m^{-2} , in the control (gray contours) and the response to 2-K SST warming (shaded contours), in (top) RAS and (bottom) UW. The plotted domain is 30°S – 30°N , 180°W – 180°E .

MSE import that largely balances the horizontal signal. In the northeastern Sahel, this overall mechanism effectively runs away. This mechanism of the increased moisture gradient generating anomalous free tropospheric subsidence is essentially a manifestation of the upped-ante mechanism described above (Chou and Neelin 2004), but with the center of action being the free troposphere rather than the boundary layer; note that the region mean meridional winds are southerly in the boundary layer and northerly above to at least 300 hPa (Figs. 12b,e).⁴

b. UW

Like RAS, the largest term in the Sahel region mean anomalous column MSE budget is the time-mean horizontal advection (7.2 W m^{-2} ; Table 2). The profiles of both anomalous time-mean advection terms in UW—and their contributions from the thermodynamic, dynamic, and covarying terms—resemble smaller-magnitude versions of their RAS counterparts (Figs. 5, 6, 10, and 8), including the dominance of the thermodynamic component of the anomalous horizontal advection in the free troposphere. Being much smaller in UW than RAS, it requires less compensating subsidence and thus poses a smaller drying influence, most notably in the midtroposphere, where, like RAS, moist static stability is smallest and therefore ascent must be largest to generate a given vertical MSE advection value. Therefore, understanding

the difference in the midtropospheric MSE gradient responses is crucial.

Figure 12 shows the control, +2 K, and response profiles in RAS and UW of the Sahel region-mean meridional MSE gradient, as well as zonal wind and meridional wind. Whereas the horizontal wind fields are largely similar across RAS and UW and respond modestly, the meridional MSE gradient is enhanced more in RAS than in UW at most levels, including the midtroposphere. Moreover, climatologically it is larger in magnitude near the surface in RAS and extends deeper into the free troposphere—zero crossings in the respective model variants are ~ 300 and ~ 450 hPa. These features lead to the following hypothesis: because of deeper climatological convection in the Sahel and equatorial Africa in RAS, the additional water vapor generated by the SST warming is communicated over a greater tropospheric depth in RAS than in UW within convecting regions. This causes the increase in the midtropospheric MSE gradient in the Sahel to be greater in RAS, necessitating greater anomalous subsidence.

One complicating factor is the role of the net energetic source term, which responds weakly in the free troposphere in RAS but not in UW (Figs. 5a,d). Figure 6c shows the anomalous vertical motion predicted by (3) applied to UW, for which it generally does a poor job, including excessive anomalous subsidence in the free troposphere. At these levels in UW, the net energetic source term largely balances the anomalous horizontal advection, thereby necessitating less sinking.

6. Uniform SST perturbations over a wide range

To further probe the relationships among the large-scale circulation, convective formulation, and precipitation in

⁴ An analogous modification of an existing, boundary layer-focused theory in order to account for free-tropospheric processes is performed by Shekhar and Boos (2016), who find that the well-known estimate for the location of the ITCZ as the latitude of the maximum near-surface MSE (Privé and Plumb 2007) is improved if the maximum of MSE averaged upward to 500 hPa is used instead.

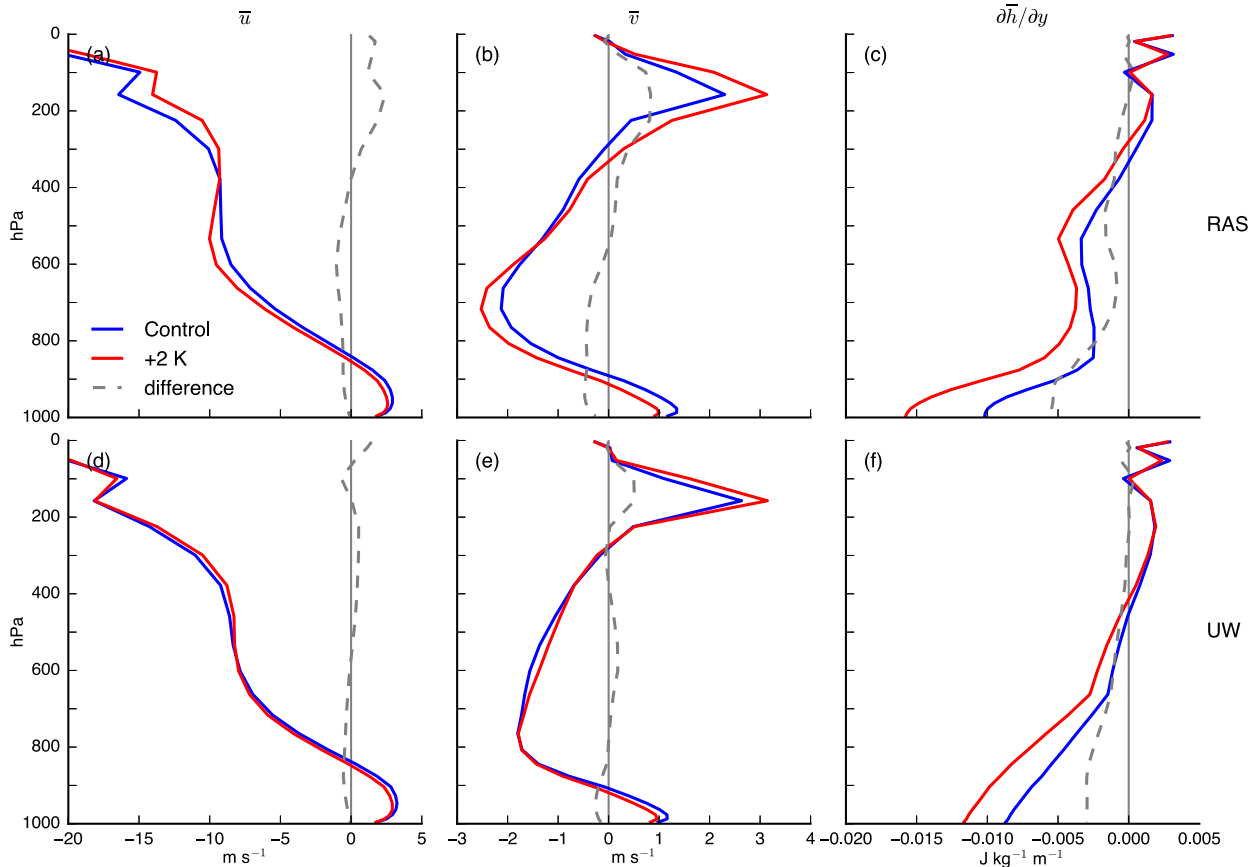


FIG. 12. Sahel region-mean profiles of (left) zonal wind (in m s^{-1}), (middle) meridional wind (in m s^{-1}), and (right) meridional MSE gradient (in $\text{J kg}^{-1} \text{s}^{-1}$), in (top) RAS and (bottom) UW.

the Sahel, we perform additional uniform SST perturbation simulations in RAS and UW with magnitudes ± 2 , ± 4 , ± 6 , ± 8 , and ± 10 K. In RAS, we also perform ± 0.25 , ± 0.5 , ± 1 , ± 1.5 , ± 3 K, and -15 K simulations. Other than the SST perturbation value, these simulations are identical to the present-day and $+2$ -K simulations, although for expediency the column-integrated MSE advection terms in this section are computed directly from monthly data without the budget-closure adjustment procedure.

Figure 13 shows, for RAS, Sahel $P - E$ as a function of various other region-mean quantities in these simulations, with each simulation's color corresponding to the imposed SST perturbation. Near present-day SSTs, Sahel $P - E$ varies linearly and rapidly with global-mean SST and local surface temperature (Fig. 13a), with an average rate of -1.1 mm day^{-1} per K of imposed SST warming. The responses of $P - E$ and several other fields taper off sharply near 1.5 K cooler and 1.5 K warmer than present-day, an explanation for which we leave for future work. Except for the very large magnitude SST simulations, evaporation scales linearly with

precipitation (not shown), such that $P - E$ largely tracks P (Fig. 13b). $P - E$ also varies linearly with the column-averaged relative humidity, which decreases with SST over nearly the full range of simulations (Fig. 13c) and is largely a positive function of column-averaged cloud fraction and ascent (Figs. 13d,e). $P - E$ varies monotonically with the average meridional MSE gradient (which becomes more negative with SST warming; Fig. 13f), column-integrated horizontal MSE advection (more positive with SST warming; Fig. 13g), and column-integrated vertical MSE advection (more negative with SST warming; Fig. 13h). In contrast, the Sahel region-mean energetic forcing is nonmonotonic both with $P - E$ and the imposed SST warming (Fig. 13i). These results support the notion that the increasing moisture difference between the Sahel and the Sahara with warming constitutes the dominant drying influence in the Sahel, which for RAS manifests in all hydrological quantities examined.

Figure 14 repeats Fig. 13 for UW. It can be seen that $P - E$ decreases monotonically with SST (Fig. 14a) and varies with most fields in largely the same manner as in

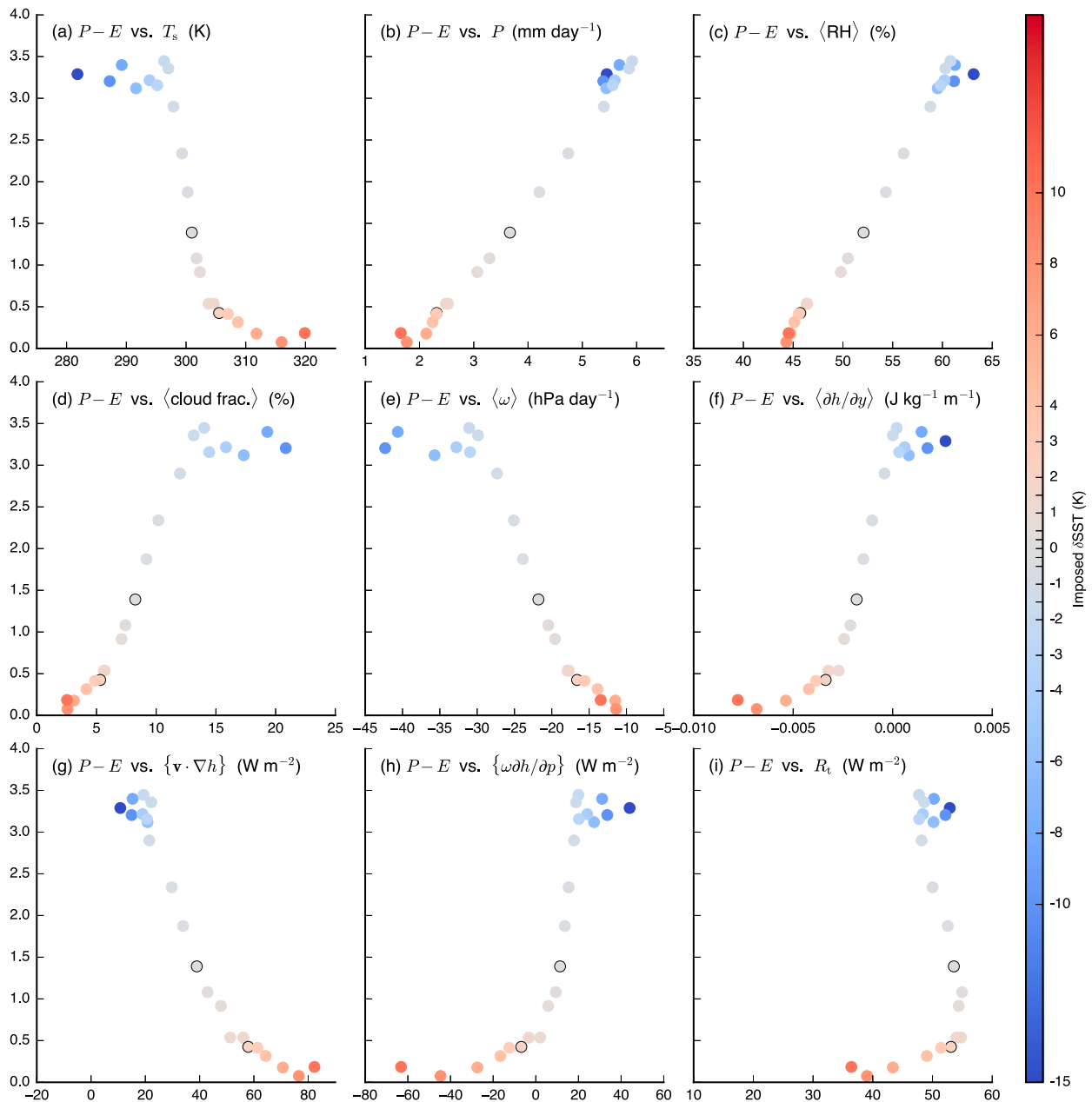


FIG. 13. Sahel region-mean precipitation as a function of various other Sahel region-mean quantities in simulations in RAS over which the uniform SST perturbation is varied from -15 to $+10$ K. Each dot represents one simulation, with their color signifying the imposed SST perturbation according to the color bar. The control and $+2$ -K simulations are outlined in black for ease of reference. Precipitation is on the vertical axis in all panels, in mm day^{-1} . The quantity on the horizontal axis is printed at the top of the axis, along with its units. Angle brackets denote column averages, and curly brackets denote column integrals.

RAS: $P - E$ decreases with the Sahel–Sahara MSE difference (Fig. 14f) and horizontal MSE advection (Fig. 14g) and increases with vertical MSE advection, relative humidity, cloud fraction, and ascent (Figs. 14c,d,e,h). However, column-average ascent and column-integrated vertical MSE advection vary over a much narrower range in UW than in RAS, despite similar ranges in all other

fields. Energetic forcing responds more clearly in UW than in RAS, increasing with warming over most of the simulations (Fig. 14i).

Unlike $P - E$, precipitation decreases with SST in the range -10 to -4 K from 3.1 to 2.5 mm day^{-1} and increases with SST in all warmer simulations up to 3.5 mm day^{-1} (Fig. 14b). To better understand this

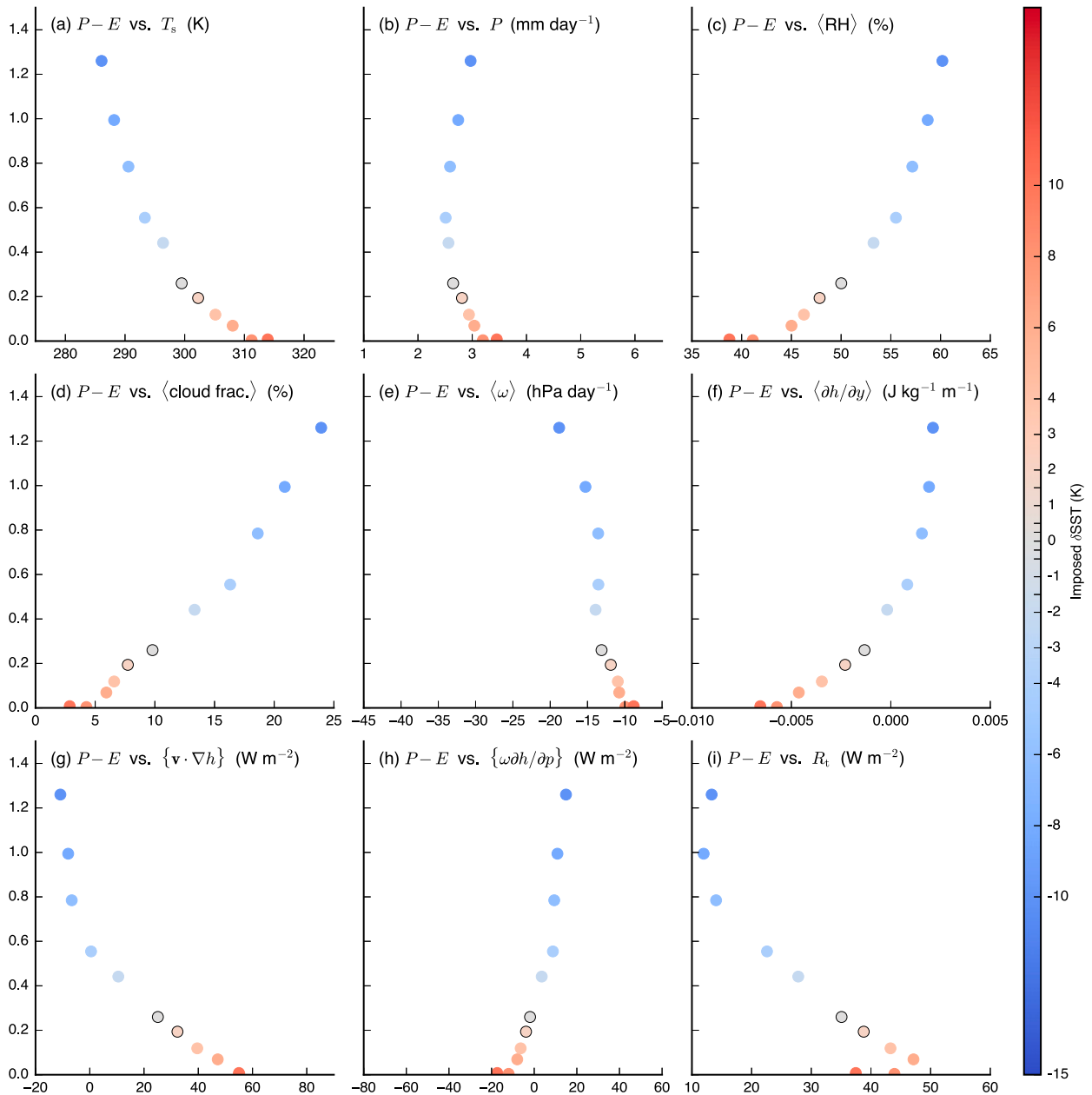


FIG. 14. As in Fig. 13, but for UW; $P - E$ in simulations in UW over which the uniform SST perturbation is varied from -10 to $+10$ K. Each dot represents one simulation, with their color signifying the imposed SST perturbation according to the color bar. The control and $+2$ -K simulations are outlined in black for ease of reference; $P - E$ is on the vertical axis in all panels, in mm day^{-1} . The quantity on the horizontal axis is printed at the top of the axis, along with its units. Angle brackets denote column averages, and curly brackets denote column integrals. The horizontal span of each panel is identical to the corresponding one in Fig. 13.

idiosyncratic precipitation behavior, we have separated the total precipitation in each simulation as before into contributions from the convective and large-scale modules (not shown). Convective precipitation in RAS and large-scale precipitation in both model variants decrease monotonically with SST (with the large scale asymptoting toward zero at SSTs warmer than

present-day in both cases). Consequently, the relationships between large-scale precipitation in UW with other fields largely adhere to expectation, resembling those of total precipitation in RAS and $P - E$ in both model variants. The large-scale cloud scheme, although more nuanced than simply raining out moisture in excess of saturation, ultimately depends closely on relative

humidity. Given the tendency for reduced relative humidity over tropical land with warming, it is therefore not surprising that large-scale cloud cover and precipitation decrease steadily with warming. The outlier is the convective precipitation in UW, which *increases* quite linearly with SST over the full -10 - to $+10$ -K range, from 0.3 to 3.2 mm day^{-1} , despite the various intensifying drying influences already described.

Another idiosyncrasy in UW is that evaporation—which increases linearly over the full -10 - to $+10$ -K range from 1.7 to 3.5 mm day^{-1} (not shown)—increases at an even faster rate with SSTs than does precipitation in the present-day and warmer simulations, such that precipitation increases while $P - E$ asymptotes toward zero. As previously noted, the expectation for a semiarid region is for evaporation to scale with precipitation at some fractional rate less than unity. This broadly occurs in RAS: the reduced moisture supply from precipitation drives reduced evaporation, and this moisture limitation dominates over the countering effects of reduced relative humidity (which increases the evaporative demand) and cloud cover (which increases the net radiation impinging on the surface). Note that the land model formulation is identical in the two model variants. This may relate to the response of the convective moistening term within the boundary layer (not shown): in UW, at least for the $+2$ -K case, SST warming generates anomalous convective drying in the boundary layer; all else equal, this would increase the evaporative demand. The response is opposite in RAS: boundary layer convective moistening is enhanced with 2 -K SST warming.

Overall, the results of these wide SST range simulations suggest that the dominant influences on the Sahel with SST warming with either convective parameterization are the increased moisture and MSE differences between the Sahel and the Sahara; acted upon by prevailing northerly flow, this enhances the advection of dry, low-MSE air into the Sahel, driving $P - E$ toward its maximally dry value of zero. However, a given increase in horizontal dry advection generates greater anomalous descent and consequently anomalous MSE import by the divergent circulation in RAS than in UW, for which we have presented an explanation for near-present-day cases in the preceding section in terms of the horizontal advection in the midtroposphere. As a result, in simulations with UW with SSTs close to or warmer than present day, the overall wettening influences of SST warming—most conspicuously increased boundary layer temperature and moisture—counteract the drying influence within the convective parameterization, yielding increased total precipitation.

7. Discussion

a. Potential direct influences of convective processes on the response to ocean warming

The discrepancy between convective precipitation responses in UW and RAS warrants consideration of the potential direct influences of the convective formulations. Zhao (2014) makes arguments of relevance regarding how entrainment will respond to warming in each convective parameterization. In RAS, each plume's entrainment rate is computed inversely based on the plume's buoyancy and its specified cloud-top height. To the extent that buoyancy [as measured by convectively available potential energy (CAPE)] increases with global warming (Singh and O'Gorman 2013; Seeley and Romps 2015) this will lead to increased entrainment with warming, a drying influence. Conversely, in UW entrainment is inversely proportional to convective depth. Given the general expectation for increased convective depths with warming (Singh and O'Gorman 2012), this will reduce entrainment, a wettening influence. Simulations with varied entrainment settings in each parameterization may clarify this issue, although resulting changes in the large-scale circulation would need to be taken into account. If entrainment did play a dominant role in UW, the expectation would be for the convective precipitation to be larger the lower the GFDL-specific land-ocean entrainment ratio (see section 2) is; in the limiting case of zero entrainment, the relative humidity of the atmosphere is irrelevant, since there is no mixing. This is qualitatively consistent with the Sahel precipitation response being more muted in the standard resolution version of HiRAM, which uses a larger ratio of 0.75 (not shown). However, the different resolutions also gives rise to other potentially confounding factors.

The cloud-base mass flux closures of the two convective parameterizations may also be important. RAS uses a CAPE-based closure, and as just noted CAPE generally increases in SST warming simulations. But this would, all else equal, act to intensify moist convection and therefore act against the simulated drying and reduced convective mass flux (not shown). The closure for UW depends on the convective inhibition and on the boundary layer eddy kinetic energy. To our knowledge, the behavior of each of these factors with warming is less well understood than CAPE.

Cloud microphysical formulations may also be relevant. In the implementation of RAS in AM2.1, precipitation efficiency (the fraction of cloud condensate that is precipitated out) is fixed at 0.975 for clouds detraining above 500 hPa and 0.5 for clouds detraining below 800 hPa (and linearly interpolated in between)

(GFDL Global Atmospheric Model Development Team 2004). As convection shallows, therefore, precipitation efficiency necessarily decreases, leaving more condensate to the large-scale scheme. But as temperature increases and relative humidity decreases, the large-scale scheme has a harder time reaching saturation. All else equal, this would act to reduce the convective and total precipitation. In contrast, the GFDL implementation of UW employs simple threshold removal of condensate, wherein all condensate exceeding some fixed threshold is precipitated out (Zhao et al. 2009). This threshold is a global constant (1 g kg^{-1}) and therefore would not contribute a positive feedback on precipitation changes like the one just proposed for RAS.

b. Relation to prior theoretical arguments

In our simulations, anomalous drying through horizontal advection in the 2-K SST warming simulation occurs throughout the free troposphere. We have argued that the midtropospheric portion of this is most effective at inhibiting precipitation, due to the shape of the climatological moist static stability and assuming a negligible response by the forcing term (which, importantly, is appropriate for RAS but not UW). This maximal efficacy of midtropospheric drying is qualitatively consistent with the single column model simulations with parameterized convection run in weak temperature gradient mode of Sobel and Bellon (2009), wherein precipitation is suppressed more by drying imposed in the midtroposphere than either the lower or upper free troposphere. However, in analogous simulations in a cloud-resolving model, drying imposed in the *lower* free troposphere is most effective at inhibiting the surface precipitation flux (Wang and Sobel 2012). The seeming implication is that the convective parameterizations are insufficiently sensitive to environmental humidity. Recalling that in UW entrainment is artificially suppressed over land to generate sufficient climatological continental precipitation, this is qualitatively consistent with UW's response.

One potentially important difference between the two control climates besides the Sahelian convective depths is the near-surface MSE field. The region of large near-surface MSE values within the Sahel is larger magnitude, more widespread, and more continental in RAS than in UW. To the extent that prevailing MSE gradients are enhanced with warming (Boos and Hurley 2013), this itself would lead to greater MSE increases in RAS than in UW.

Despite the modest changes in moist static stability in our simulations, dry static stability does increase appreciably (not shown), and prior work has argued that

increased upper-tropospheric dry static stability with warming inhibits convection in the Sahel (Giannini 2010). This is consistent with our results. Conversely, the strength of the Sahara heat low circulation—which numerous studies argue is strengthened with warming, thereby enhancing the monsoon flow into the Sahel (e.g., Biasutti et al. 2009)—is not of central importance in these simulations. Although Saharan surface warming is modestly higher in UW than RAS, in both cases the anomalous boundary layer flow in the northern Sahel is northerly, opposite to the expectation if an anomalous heat low circulation centered in the Sahara Desert was dominant.

We find no significant role for anomalous Rossby wave signals emanating from South Asia (i.e., the Rodwell–Hoskins mechanism; Rodwell and Hoskins 1996) in modulating Sahelian rainfall in either model variant. The eddy streamfunction shows no clear anomalous Rossby wave signal emanating from South Asia in the +2-K simulations, and in RAS while Sahelian precipitation decreases monotonically across the wide SST range simulations, South Asian precipitation is nonmonotonic, with a minimum near present day and greater values in both the warming and cooling simulations (not shown).

8. Summary

Wet-season rainfall in the Sahel decreases by 40% in response to uniform 2-K SST warming in AM2.1 when the default RAS convective parameterization is used but increases by 6% when the UW parameterization is used instead. The control climate is also drier and cooler when using UW. We attempt to understand these sensitivities through the column-integrated MSE budget.

In both model variants, the present-day control simulation budget broadly comprises positive net energetic forcing balanced by horizontal advection of dry, low-MSE Saharan air into the northern Sahel and export of MSE by deep moist convection in the southern Sahel, with additional region-mean MSE export from transient eddies. In RAS, the time-mean divergent circulation exports MSE in the southern Sahel but imports MSE in the northern Sahel due to the convection shallowing moving northward, leading to a near-zero column mean MSE export through the divergent circulation. In UW, ascent is generally shallower, such that the divergent circulation imports MSE throughout the Sahel. Thus, in either case the region is far from the canonical tropical convecting zone balance between net energetic forcing and MSE export by the time-mean divergent circulation. The

hydrological and thermal imprints in the control simulations of this difference in divergent circulation strength are less convective precipitation, more low cloud, and cooler surface temperatures in UW compared to RAS.

In RAS, the severe reduction in Sahelian rainfall with SST warming is the hydrological imprint of a marked shallowing of convection and of the associated divergent circulation; these are driven by enhanced horizontal advection of dry, low-MSE Saharan air. This leads to an expression for the anomalous vertical motion in the free troposphere in terms of the climatological moist static stability and the change in the meridional gradient of MSE. Changes in the MSE gradient are especially important in the midtroposphere, where the moist static stability is small and therefore ascent must respond strongly to balance a given horizontal MSE advection anomaly. In UW, the horizontal MSE gradient is not enhanced as much in the midtroposphere, which we hypothesize arises from the shallower prevailing convection in that model variant being less effective at communicating aloft the oceanic boundary layer moistening and warming.

Varying SSTs over a wide range with either convective parameterization yields consistent energetic, $P - E$, and large-scale precipitation responses but differing convective and total precipitation responses: the advection of dry, low-MSE air from the Sahara desert is steadily enhanced with warming, but in terms of precipitation in UW this is overcome by the broader wetting influences in climatological convecting regions that accompany SST warming. In both RAS and UW, large-scale precipitation asymptotes toward zero in the warmest simulations. In RAS, convective precipitation decreases with warming. In UW, increased convective precipitation with warming exceeds the decreased large-scale precipitation, at least for simulations near present day and warmer, and evaporation increases faster than does precipitation, leading to $P - E$ approaching zero. Although these idiosyncrasies relating to convective physics in UW remain under investigation, we expect the increased meridional MSE gradient with warming, which stems from well-understood physical principles, to figure centrally in the Sahel hydrological response to mean SST change in other models as well.

Acknowledgments. We thank Bill Boos, Usama Anber, and Kirsten Findell for their insightful reviews of earlier drafts and three anonymous reviewers. We thank Leo Donner for scientific guidance, Spencer Clark for guidance on computational procedures, and Lucas Harris for guidance on numerical techniques and model

conservation properties. S.A.H. was supported during the majority of this work by a Department of Defense National Defense Science and Engineering Graduate Fellowship at Princeton University and by a National Science Foundation Postdoctoral Research Fellowship during the final stages.

APPENDIX A

Adjustment Method for Correcting Imbalances in Column Tracer Budgets

a. Motivation

The interpolation of GCM and reanalysis data from their model-native coordinates to regular latitude–longitude grids and/or pressure levels generates spurious imbalances in the budgets of mass and other conserved tracers (Trenberth 1991). This is especially true over land, where topography induces sharp gradients of surface pressure. As a result, commonly used finite-differencing methods for the derivatives in the flux divergence terms can yield residuals $>100 \text{ W m}^{-2}$ at individual grid points in the column MSE budget. Here we present a post hoc adjustment method that rectifies these imbalances. It is effectively an extension of the dry mass budget adjustment method introduced by Trenberth (1991) and is similar to that of Peters et al. (2008). Kidson and Newell (1977) also present a similar method for column mass using analysis data.

b. Adjustment procedure

Neglecting diffusion, the column-integrated budget of a conserved tracer, m , comprises time-tendency, flux divergence, and source terms:

$$\frac{\partial \{m\}}{\partial t} + \nabla \cdot \{m\mathbf{v}\} = S, \quad (\text{A1})$$

where curly brackets denote a mass-weighted column integral ($\{ \} = \int_0^{p_s} dp/g$, where p_s is surface pressure), S is the column-integrated source minus sink, and \mathbf{v} is the true horizontal wind such that this equality holds exactly. Using model-postprocessed data introduces a nonzero residual, R :

$$\frac{\partial \{m\}}{\partial t} + \nabla \cdot \{m\mathbf{v}_{\text{raw}}\} = S + R, \quad (\text{A2})$$

where \mathbf{v}_{raw} is the unadjusted horizontal wind, which we have assumed is the source of all error (rather than the time tendency or source terms). Let \mathbf{v}_{adj} be the adjustment applied to the wind, signed such that

$$\mathbf{v} = \mathbf{v}_{\text{raw}} - \mathbf{v}_{\text{adj}}. \quad (\text{A3})$$

Combining (A2) and (A3) yields

$$\nabla \cdot \{m \mathbf{v}_{\text{adj}}\} = R. \quad (\text{A4})$$

We assume that the adjustment is barotropic, such that it can be pulled out of the column integral. We also assume that the adjustment field is irrotational. This results in a system of two equations,

$$\begin{aligned} \nabla \cdot (\{m\} \mathbf{v}_{\text{adj}}) &= R, \\ \nabla \times (\{m\} \mathbf{v}_{\text{adj}}) &= 0, \end{aligned} \quad (\text{A5})$$

which can be solved (e.g., using spherical harmonics) for the zonal and meridional components of the quantity $\{m\} \mathbf{v}_{\text{adj}}$. By subsequently dividing by $\{m\}$ to get \mathbf{v}_{adj} and, finally, using (A3), we arrive at the adjusted wind \mathbf{v} that exactly satisfies the column budget expression (A1).

c. Caveats

Importantly, this procedure will generate a horizontal wind field that yields closure of the specified source and time-tendency terms, whether or not such closure is physically justified. Most significantly, if this were applied to the MSE budget using monthly-mean data, then the resulting adjusted monthly-mean circulation would exactly balance the energy storage and net energetic forcing terms, with the likely false implication that transient eddies have no contribution.

While the resulting adjusted wind field is defined at each vertical level, the adjustment itself is barotropic and based on column-integrated terms, and closure is ensured only in the column integral, not at each individual level.

APPENDIX B

Computational Procedure Used for Each Term in the Moist Static Energy Budget

a. Column-integrated moist static energy flux divergence at each time step

We apply two consecutive adjustments, first correcting column total mass (dry air plus water vapor) and then column energy. The column mass adjustment is based on the expression

$$\frac{\partial p_s}{\partial t} + \nabla \cdot \int_0^{p_s} \mathbf{v} dp = g(E - P). \quad (\text{B1})$$

This corrects for column mass imbalances exactly and largely ameliorates column energy imbalances. We then repeat this procedure, starting with these mass-adjusted winds, applied to the column MSE budget

$$\frac{\partial}{\partial t} \{\mathcal{E}\} + \nabla \cdot \{h \mathbf{v}\} = F_{\text{net}}, \quad (\text{B2})$$

with symbols all defined as in the main text. We apply this two-step adjustment to the horizontal wind field at each time step of the postprocessed model data. The column MSE flux divergence is then computed by forming the MSE fluxes ($h \mathbf{v}$), integrating them over the entire column ($\{h \mathbf{v}\}$), and then again using spherical harmonics to compute the divergence of the column integrals ($\nabla \cdot \{h \mathbf{v}\}$). This procedure yields the column-integrated MSE flux divergence in nearly exact balance with the column net energetic forcing and time tendency at each 3-hourly time step.

b. Partitioning total flux divergence into eddy and time-mean components

From this 3-hourly adjusted column flux divergence field, we separate the eddy and time-mean components as standard. Namely, the adjusted winds and all other original fields are averaged within each month, and the column flux divergence is recomputed using these fields to get $\nabla \cdot \{\bar{h} \bar{\mathbf{v}}\}$. The eddy component is then computed by subtracting the time-mean field from the full field: $\nabla \cdot \{h' \mathbf{v}'\} = \nabla \cdot \{h \mathbf{v}\} - \nabla \cdot \{\bar{h} \bar{\mathbf{v}}\}$.

c. Partitioning time-mean advection into horizontal and vertical components

We partition the total time-mean column flux divergence into horizontal and vertical advection components by 1) explicitly computing the horizontal advection at each level, 2) column-integrating, and 3) subtracting that integral from the time mean to get the vertical advection as a residual. The level-by-level horizontal advection computation uses the time series of adjusted, monthly-mean horizontal winds and second-order, upwind finite differencing. Because the data are on the model-native hybrid pressure-sigma coordinates (Simmons and Burridge 1981) while the budget equations require horizontal gradients on constant pressure surfaces, additional terms are required (Peters et al. 2008):

$$\nabla_p \bar{h} = \nabla_\eta \bar{h} + \frac{\partial \bar{h}}{\partial \eta} \nabla_p \eta = \nabla_\eta \bar{h} - \frac{\partial \bar{h}}{\partial \eta} \frac{b}{a' + b' \bar{p}_s} \nabla_\eta \bar{p}_s, \quad (\text{B3})$$

where the hybrid sigma-pressure model coordinates η are terrain-following near the surface and transition to constant pressure surfaces near the model top: $p(\eta, p_s) = a(\eta) + b(\eta)p_s$, where a and b do not vary horizontally or in time, $a' \equiv da/d\eta$, and $b' \equiv db/d\eta$ (see Table 2 of GFDL Global Atmospheric Model Development Team 2004).

d. Vertical advection at individual vertical levels

To examine the vertical profile of the budget terms, we also compute the time-mean vertical advection explicitly at each level using second-order upwind finite differencing. These are the quantities shown in all profile plots of time-mean advection. The sum of the two explicitly computed advection terms, column-integrated, exhibits a region-mean residual of $\sim 10 \text{ W m}^{-2}$ compared to the total time-mean flux divergence. But the overall character and spatial patterns of the column vertical advection is similar between the two methods.

This is why the total region-mean change differs modestly between the previously quoted value and the sum of the three response decomposition terms (-15.9 and -18.8 W m^{-2} , respectively). Similarly, to compute the decomposition terms only, for expediency the horizontal advection is computed using monthly averaged data, unadjusted. The results appear qualitatively insensitive to this choice.

e. Time tendency and source terms

Time tendencies are computed by first integrating the tracer over the column and then applying second-order centered finite differencing at each time step. The source terms are outputted directly by the model and require no subsequent manipulation.

REFERENCES

- Arakawa, A., and W. H. Schubert, 1974: Interaction of a cumulus cloud ensemble with the large-scale environment, Part I. *J. Atmos. Sci.*, **31**, 674–701, doi:[10.1175/1520-0469\(1974\)031<0674:IOACCE>2.0.CO;2](https://doi.org/10.1175/1520-0469(1974)031<0674:IOACCE>2.0.CO;2).
- Back, L. E., and C. S. Bretherton, 2006: Geographic variability in the export of moist static energy and vertical motion profiles in the tropical Pacific. *Geophys. Res. Lett.*, **33**, L17810, doi:[10.1029/2006GL026672](https://doi.org/10.1029/2006GL026672).
- Berg, A., and Coauthors, 2015: Interannual coupling between summertime surface temperature and precipitation over land: Processes and implications for climate change. *J. Climate*, **28**, 1308–1328, doi:[10.1175/JCLI-D-14-00324.1](https://doi.org/10.1175/JCLI-D-14-00324.1).
- Bernstein, D. N., and J. D. Neelin, 2016: Identifying sensitive ranges in global warming precipitation change dependence on convective parameters. *Geophys. Res. Lett.*, **43**, 5841–5850, doi:[10.1002/2016GL069022](https://doi.org/10.1002/2016GL069022).
- Biasutti, M., 2013: Forced Sahel rainfall trends in the CMIP5 archive. *J. Geophys. Res. Atmos.*, **118**, 1613–1623, doi:[10.1002/jgrd.50206](https://doi.org/10.1002/jgrd.50206).
- , I. M. Held, A. H. Sobel, and A. Giannini, 2008: SST forcings and Sahel rainfall variability in simulations of the twentieth and twenty-first centuries. *J. Climate*, **21**, 3471–3486, doi:[10.1175/2007JCLI1896.1](https://doi.org/10.1175/2007JCLI1896.1).
- , A. H. Sobel, and S. J. Camargo, 2009: The role of the Sahara low in summertime Sahel rainfall variability and change in the CMIP3 models. *J. Climate*, **22**, 5755–5771, doi:[10.1175/2009JCLI2969.1](https://doi.org/10.1175/2009JCLI2969.1).
- Birch, C. E., D. J. Parker, J. H. Marsham, D. Copsey, and L. Garcia-Carreras, 2014: A seamless assessment of the role of convection in the water cycle of the West African monsoon. *J. Geophys. Res. Atmos.*, **119**, 2890–2912, doi:[10.1002/2013JD020887](https://doi.org/10.1002/2013JD020887).
- Boos, W. R., and J. V. Hurley, 2013: Thermodynamic bias in the multimodel mean boreal summer monsoon. *J. Climate*, **26**, 2279–2287, doi:[10.1175/JCLI-D-12-00493.1](https://doi.org/10.1175/JCLI-D-12-00493.1).
- Bretherton, C. S., J. R. McCaa, and H. Grenier, 2004: A new parameterization for shallow cumulus convection and its application to marine subtropical cloud-topped boundary layers. Part I: Description and 1D results. *Mon. Wea. Rev.*, **132**, 864–882, doi:[10.1175/1520-0493\(2004\)132<0864:ANPFSF>2.0.CO;2](https://doi.org/10.1175/1520-0493(2004)132<0864:ANPFSF>2.0.CO;2).
- , P. N. Blossey, and M. E. Peters, 2006: Interpretation of simple and cloud-resolving simulations of moist convection–radiation interaction with a mock-Walker circulation. *Theor. Comput. Fluid Dyn.*, **20**, 421–442, doi:[10.1007/s00162-006-0029-7](https://doi.org/10.1007/s00162-006-0029-7).
- Byrne, M. P., and P. A. O’Gorman, 2013a: Land–ocean warming contrast over a wide range of climates: Convective quasi-equilibrium theory and idealized simulations. *J. Climate*, **26**, 4000–4016, doi:[10.1175/JCLI-D-12-00262.1](https://doi.org/10.1175/JCLI-D-12-00262.1).
- , and —, 2013b: Link between land–ocean warming contrast and surface relative humidities in simulations with coupled climate models. *Geophys. Res. Lett.*, **40**, 5223–5227, doi:[10.1002/grl.50971](https://doi.org/10.1002/grl.50971).
- Chadwick, R., 2016: Which aspects of CO₂ forcing and SST warming cause most uncertainty in projections of tropical rainfall change over land and ocean? *J. Climate*, **29**, 2493–2509, doi:[10.1175/JCLI-D-15-0777.1](https://doi.org/10.1175/JCLI-D-15-0777.1).
- Charney, J. G., 1975: Dynamics of deserts and drought in the Sahel. *Quart. J. Roy. Meteor. Soc.*, **101**, 193–202, doi:[10.1002/qj.49710142802](https://doi.org/10.1002/qj.49710142802).
- , P. H. Stone, and W. J. Quirk, 1975: Drought in the Sahara: A biogeophysical feedback mechanism. *Science*, **187**, 434–435, doi:[10.1126/science.187.4175.434](https://doi.org/10.1126/science.187.4175.434).
- Chou, C., and J. D. Neelin, 2004: Mechanisms of global warming impacts on regional tropical precipitation. *J. Climate*, **17**, 2688–2701, doi:[10.1175/1520-0442\(2004\)017<2688:MOGWIO>2.0.CO;2](https://doi.org/10.1175/1520-0442(2004)017<2688:MOGWIO>2.0.CO;2).
- , —, and H. Su, 2001: Ocean–atmosphere–land feedbacks in an idealized monsoon. *Quart. J. Roy. Meteor. Soc.*, **127**, 1869–1891, doi:[10.1002/qj.49712757602](https://doi.org/10.1002/qj.49712757602).
- Collins, M., and Coauthors, 2013: Long-term climate change: Projections, commitments and irreversibility. *Climate Change 2013: The Physical Science Basis*, T. F. Stocker et al., Eds., Cambridge University Press, 1029–1136, doi:[10.1017/CBO9781107415324.024](https://doi.org/10.1017/CBO9781107415324.024).
- Cook, K. H., 1994: Mechanisms by which surface drying perturbs tropical precipitation fields. *J. Climate*, **7**, 400–413, doi:[10.1175/1520-0442\(1994\)007<0400:MBWSDP>2.0.CO;2](https://doi.org/10.1175/1520-0442(1994)007<0400:MBWSDP>2.0.CO;2).
- , 1997: Large-scale atmospheric dynamics and Sahelian precipitation. *J. Climate*, **10**, 1137–1152, doi:[10.1175/1520-0442\(1997\)010<1137:LSADAS>2.0.CO;2](https://doi.org/10.1175/1520-0442(1997)010<1137:LSADAS>2.0.CO;2).
- , and E. K. Vizy, 2006: Coupled model simulations of the West African monsoon system: Twentieth- and twenty-first-century simulations. *J. Climate*, **19**, 3681–3703, doi:[10.1175/JCLI3814.1](https://doi.org/10.1175/JCLI3814.1).
- Delworth, T. L., and Coauthors, 2006: GFDL’s CM2 global coupled climate models. Part I: Formulation and simulation characteristics. *J. Climate*, **19**, 643–674, doi:[10.1175/JCLI3629.1](https://doi.org/10.1175/JCLI3629.1).
- Dong, B., and R. Sutton, 2015: Dominant role of greenhouse-gas forcing in the recovery of Sahel rainfall. *Nat. Climate Change*, **5**, 757–760, doi:[10.1038/nclimate2664](https://doi.org/10.1038/nclimate2664).
- Donner, L. J., and Coauthors, 2011: The dynamical core, physical parameterizations, and basic simulation characteristics of the atmospheric component AM3 of the GFDL global

- coupled model CM3. *J. Climate*, **24**, 3484–3519, doi:[10.1175/2011JCLI3955.1](https://doi.org/10.1175/2011JCLI3955.1).
- Folland, C. K., T. N. Palmer, and D. E. Parker, 1986: Sahel rainfall and worldwide sea temperatures, 1901–85. *Nature*, **320**, 602–607, doi:[10.1038/320602a0](https://doi.org/10.1038/320602a0).
- Frierson, D. M. W., 2007: The dynamics of idealized convection schemes and their effect on the zonally averaged tropical circulation. *J. Atmos. Sci.*, **64**, 1959–1976, doi:[10.1175/JAS3935.1](https://doi.org/10.1175/JAS3935.1).
- Gallego, D., P. Ordóñez, P. Ribera, C. Peña-Ortiz, and R. García-Herrera, 2015: An instrumental index of the West African monsoon back to the nineteenth century. *Quart. J. Roy. Meteor. Soc.*, **141**, 3166–3176, doi:[10.1002/qj.2601](https://doi.org/10.1002/qj.2601).
- GFDL Global Atmospheric Model Development Team, 2004: The New GFDL Global Atmosphere and Land Model AM2–LM2: Evaluation with prescribed SST simulations. *J. Climate*, **17**, 4641–4673, doi:[10.1175/JCLI-3223.1](https://doi.org/10.1175/JCLI-3223.1).
- Giannini, A., 2010: Mechanisms of climate change in the semiarid African Sahel: The local view. *J. Climate*, **23**, 743–756, doi:[10.1175/2009JCLI3123.1](https://doi.org/10.1175/2009JCLI3123.1).
- , R. Saravanan, and P. Chang, 2003: Oceanic forcing of Sahel rainfall on interannual to interdecadal time scales. *Science*, **302**, 1027–1030, doi:[10.1126/science.1089357](https://doi.org/10.1126/science.1089357).
- , S. Salack, T. Lodoun, A. Ali, A. T. Gaye, and O. Ndiaye, 2013: A unifying view of climate change in the Sahel linking intra-seasonal, interannual and longer time scales. *Environ. Res. Lett.*, **8**, 024010, doi:[10.1088/1748-9326/8/2/024010](https://doi.org/10.1088/1748-9326/8/2/024010).
- Hales, K., J. D. Neelin, and N. Zeng, 2006: Interaction of vegetation and atmospheric dynamical mechanisms in the mid-Holocene African monsoon. *J. Climate*, **19**, 4105–4120, doi:[10.1175/JCLI3833.1](https://doi.org/10.1175/JCLI3833.1).
- He, J., B. J. Soden, and B. Kirtman, 2014: The robustness of the atmospheric circulation and precipitation response to future anthropogenic surface warming. *Geophys. Res. Lett.*, **41**, 2614–2622, doi:[10.1002/2014GL059435](https://doi.org/10.1002/2014GL059435).
- Held, I. M., and B. J. Soden, 2006: Robust responses of the hydrological cycle to global warming. *J. Climate*, **19**, 5686–5699, doi:[10.1175/JCLI3990.1](https://doi.org/10.1175/JCLI3990.1).
- , T. L. Delworth, J. Lu, K. L. Findell, and T. R. Knutson, 2005: Simulation of Sahel drought in the 20th and 21st centuries. *Proc. Natl. Acad. Sci. USA*, **102**, 17 891–17 896, doi:[10.1073/pnas.0509057102](https://doi.org/10.1073/pnas.0509057102).
- Hill, S. A., 2016: Energetic and hydrological responses of Hadley circulations and the African Sahel to sea surface temperature perturbations. Ph.D. thesis, Princeton University, 186 pp.
- , Y. Ming, and I. M. Held, 2015: Mechanisms of forced tropical meridional energy flux change. *J. Climate*, **28**, 1725–1742, doi:[10.1175/JCLI-D-14-00165.1](https://doi.org/10.1175/JCLI-D-14-00165.1).
- Im, E.-S., R. L. Gianotti, and E. A. B. Eltahir, 2014: Improving the simulation of the West African monsoon using the MIT regional climate model. *J. Climate*, **27**, 2209–2229, doi:[10.1175/JCLI-D-13-00188.1](https://doi.org/10.1175/JCLI-D-13-00188.1).
- Inoue, K., and L. E. Back, 2015: Gross moist stability assessment during TOGA COARE: Various interpretations of gross moist stability. *J. Atmos. Sci.*, **72**, 4148–4166, doi:[10.1175/JAS-D-15-0092.1](https://doi.org/10.1175/JAS-D-15-0092.1).
- Kidson, J. W., and R. E. Newell, 1977: African rainfall and its relation to the upper air circulation. *Quart. J. Roy. Meteor. Soc.*, **103**, 441–456, doi:[10.1002/qj.49710343705](https://doi.org/10.1002/qj.49710343705).
- Losada, T., B. Rodríguez-Fonseca, E. Mohino, J. Bader, S. Janicot, and C. R. Mechoso, 2012: Tropical SST and Sahel rainfall: A non-stationary relationship. *Geophys. Res. Lett.*, **39**, L12705, doi:[10.1029/2012GL052423](https://doi.org/10.1029/2012GL052423).
- Lough, J. M., 1986: Tropical Atlantic sea surface temperatures and rainfall variations in sub-Saharan Africa. *Mon. Wea. Rev.*, **114**, 561–570, doi:[10.1175/1520-0493\(1986\)114<0561:TASSTA>2.0.CO;2](https://doi.org/10.1175/1520-0493(1986)114<0561:TASSTA>2.0.CO;2).
- Lu, J., 2009: The dynamics of the Indian Ocean sea surface temperature forcing of Sahel drought. *Climate Dyn.*, **33**, 445–460, doi:[10.1007/s00382-009-0596-6](https://doi.org/10.1007/s00382-009-0596-6).
- Marshall, J. H., N. S. Dixon, L. García-Carreras, G. M. S. Lister, D. J. Parker, P. Knippertz, and C. E. Birch, 2013: The role of moist convection in the West African monsoon system: Insights from continental-scale convection-permitting simulations. *Geophys. Res. Lett.*, **40**, 1843–1849, doi:[10.1002/grl.50347](https://doi.org/10.1002/grl.50347).
- McCrary, R. R., D. A. Randall, and C. Stan, 2014: Simulations of the West African monsoon with a superparameterized climate model. Part I: The seasonal cycle. *J. Climate*, **27**, 8303–8322, doi:[10.1175/JCLI-D-13-00676.1](https://doi.org/10.1175/JCLI-D-13-00676.1).
- Milly, P. C. D., and A. B. Shmakin, 2002: Global modeling of land water and energy balances. Part I: The Land Dynamics (LaD) model. *J. Hydrometeorol.*, **3**, 283–299, doi:[10.1175/1525-7541\(2002\)003<0283:GMOLWA>2.0.CO;2](https://doi.org/10.1175/1525-7541(2002)003<0283:GMOLWA>2.0.CO;2).
- Mitchell, J. F. B., C. A. Wilson, and W. M. Cunningham, 1987: On CO₂ climate sensitivity and model dependence of results. *Quart. J. Roy. Meteor. Soc.*, **113**, 293–322, doi:[10.1002/qj.49711347517](https://doi.org/10.1002/qj.49711347517).
- Moorthi, S., and M. J. Suarez, 1992: Relaxed Arakawa–Schubert: A parameterization of moist convection for general circulation models. *Mon. Wea. Rev.*, **120**, 978–1002, doi:[10.1175/1520-0493\(1992\)120<0978:RASAP0>2.0.CO;2](https://doi.org/10.1175/1520-0493(1992)120<0978:RASAP0>2.0.CO;2).
- Neelin, J. D., 2007: Moist dynamics of tropical convection zones in monsoons, teleconnections, and global warming. *The Global Circulation of the Atmosphere*, T. Schneider and A. H. Sobel, Eds., Princeton University Press, 267–301.
- , and I. M. Held, 1987: Modeling tropical convergence based on the moist static energy budget. *Mon. Wea. Rev.*, **115**, 3–12, doi:[10.1175/1520-0493\(1987\)115<0003:MTCBOT>2.0.CO;2](https://doi.org/10.1175/1520-0493(1987)115<0003:MTCBOT>2.0.CO;2).
- , C. Chou, and H. Su, 2003: Tropical drought regions in global warming and El Niño teleconnections. *Geophys. Res. Lett.*, **30**, 2275, doi:[10.1029/2003GL018625](https://doi.org/10.1029/2003GL018625).
- Nicholson, S. E., 1985: Sub-Saharan rainfall 1981–84. *J. Climate Appl. Meteor.*, **24**, 1388–1391, doi:[10.1175/1520-0450\(1985\)024<1388:SSR>2.0.CO;2](https://doi.org/10.1175/1520-0450(1985)024<1388:SSR>2.0.CO;2).
- , 2013: The West African Sahel: A review of recent studies on the rainfall regime and its interannual variability. *ISRN Meteor.*, 2013, e453521, doi:[10.1155/2013/453521](https://doi.org/10.1155/2013/453521).
- Nie, J., W. R. Boos, and Z. Kuang, 2010: Observational evaluation of a convective quasi-equilibrium view of monsoons. *J. Climate*, **23**, 4416–4428, doi:[10.1175/2010JCLI3505.1](https://doi.org/10.1175/2010JCLI3505.1).
- Park, J.-Y., J. Bader, and D. Matei, 2015: Northern-hemispheric differential warming is the key to understanding the discrepancies in the projected Sahel rainfall. *Nat. Commun.*, **6**, 5985, doi:[10.1038/ncomms6985](https://doi.org/10.1038/ncomms6985).
- Peters, M. E., Z. Kuang, and C. C. Walker, 2008: Analysis of atmospheric energy transport in ERA-40 and implications for simple models of the mean tropical circulation. *J. Climate*, **21**, 5229–5241, doi:[10.1175/2008JCLI2073.1](https://doi.org/10.1175/2008JCLI2073.1).
- Privé, N. C., and R. A. Plumb, 2007: Monsoon dynamics with interactive forcing. Part I: Axisymmetric studies. *J. Atmos. Sci.*, **64**, 1417–1430, doi:[10.1175/JAS3916.1](https://doi.org/10.1175/JAS3916.1).
- Reynolds, R. W., N. A. Rayner, T. M. Smith, D. C. Stokes, and W. Wang, 2002: An improved in situ and satellite SST analysis for climate. *J. Climate*, **15**, 1609–1625, doi:[10.1175/1520-0442\(2002\)015<1609:AHSAS>2.0.CO;2](https://doi.org/10.1175/1520-0442(2002)015<1609:AHSAS>2.0.CO;2).
- Rodríguez-Fonseca, B., and Coauthors, 2015: Variability and predictability of West African droughts: A review on the role of sea surface temperature anomalies. *J. Climate*, **28**, 4034–4060, doi:[10.1175/JCLI-D-14-00130.1](https://doi.org/10.1175/JCLI-D-14-00130.1).

- Rodwell, M. J., and B. J. Hoskins, 1996: Monsoons and the dynamics of deserts. *Quart. J. Roy. Meteor. Soc.*, **122**, 1385–1404, doi:[10.1002/qj.49712253408](https://doi.org/10.1002/qj.49712253408).
- Scheff, J., and D. M. W. Frierson, 2014: Scaling potential evapotranspiration with greenhouse warming. *J. Climate*, **27**, 1539–1558, doi:[10.1175/JCLI-D-13-00233.1](https://doi.org/10.1175/JCLI-D-13-00233.1).
- , and —, 2015: Terrestrial aridity and its response to greenhouse warming across CMIP5 climate models. *J. Climate*, **28**, 5583–5600, doi:[10.1175/JCLI-D-14-00480.1](https://doi.org/10.1175/JCLI-D-14-00480.1).
- Seeley, J. T., and D. M. Romps, 2015: Why does tropical convective available potential energy (CAPE) increase with warming? *Geophys. Res. Lett.*, **42**, 10 429–10 437, doi:[10.1002/2015GL066199](https://doi.org/10.1002/2015GL066199).
- Shanahan, T. M., and Coauthors, 2015: The time-transgressive termination of the African Humid Period. *Nat. Geosci.*, **8**, 140–144, doi:[10.1038/ngeo2329](https://doi.org/10.1038/ngeo2329).
- Shekhar, R., and W. R. Boos, 2016: Improving energy-based estimates of monsoon location in the presence of proximal deserts. *J. Climate*, **29**, 4741–4761, doi:[10.1175/JCLI-D-15-0747.1](https://doi.org/10.1175/JCLI-D-15-0747.1).
- Sherwood, S., and Q. Fu, 2014: A drier future? *Science*, **343**, 737–739, doi:[10.1126/science.1247620](https://doi.org/10.1126/science.1247620).
- Simmons, A. J., and D. M. Burridge, 1981: An energy and angular-momentum conserving vertical finite-difference scheme and hybrid vertical coordinates. *Mon. Wea. Rev.*, **109**, 758–766, doi:[10.1175/1520-0493\(1981\)109<0758:AEAAMC>2.0.CO;2](https://doi.org/10.1175/1520-0493(1981)109<0758:AEAAMC>2.0.CO;2).
- Singh, M. S., and P. A. O’Gorman, 2012: Upward shift of the atmospheric general circulation under global warming: Theory and simulations. *J. Climate*, **25**, 8259–8276, doi:[10.1175/JCLI-D-11-00699.1](https://doi.org/10.1175/JCLI-D-11-00699.1).
- , and —, 2013: Influence of entrainment on the thermal stratification in simulations of radiative–convective equilibrium. *Geophys. Res. Lett.*, **40**, 4398–4403, doi:[10.1002/grl.50796](https://doi.org/10.1002/grl.50796).
- Sobel, A. H., 2007: Simple models of ensemble-averaged tropical precipitation and surface wind, given the sea surface temperature. *The Global Circulation of the Atmosphere*, T. Schneider and A. H. Sobel, Eds., Princeton University Press, 219–251.
- , and G. Bellon, 2009: The effect of imposed drying on parameterized deep convection. *J. Atmos. Sci.*, **66**, 2085–2096, doi:[10.1175/2008JAS2926.1](https://doi.org/10.1175/2008JAS2926.1).
- Su, H., and J. D. Neelin, 2002: Teleconnection mechanisms for tropical Pacific descent anomalies during El Niño. *J. Atmos. Sci.*, **59**, 2694–2712, doi:[10.1175/1520-0469\(2002\)059<2694:TMFTPD>2.0.CO;2](https://doi.org/10.1175/1520-0469(2002)059<2694:TMFTPD>2.0.CO;2).
- Tanaka, M., B. C. Weare, A. R. Navato, and R. E. Newell, 1975: Recent African rainfall patterns. *Nature*, **255**, 201–203, doi:[10.1038/255201a0](https://doi.org/10.1038/255201a0).
- Thorncroft, C. D., N. M. J. Hall, and G. N. Kiladis, 2008: Three-dimensional structure and dynamics of African easterly waves. Part III: Genesis. *J. Atmos. Sci.*, **65**, 3596–3607, doi:[10.1175/2008JAS2575.1](https://doi.org/10.1175/2008JAS2575.1).
- Tokioka, T., K. Yamazaki, A. Kitoh, and T. Ose, 1988: The equatorial 30–60 day oscillation and the Arakawa–Schubert penetrative cumulus parameterization. *J. Meteor. Soc. Japan*, **66**, 883–901, doi:[10.2151/jmsj1965.66.6_883](https://doi.org/10.2151/jmsj1965.66.6_883).
- Trenberth, K. E., 1991: Climate diagnostics from global analyses: Conservation of mass in ECMWF analyses. *J. Climate*, **4**, 707–722, doi:[10.1175/1520-0442\(1991\)004<0707:CDFGAC>2.0.CO;2](https://doi.org/10.1175/1520-0442(1991)004<0707:CDFGAC>2.0.CO;2).
- Wang, S., and A. H. Sobel, 2012: Impact of imposed drying on deep convection in a cloud-resolving model. *J. Geophys. Res.*, **117**, D02112, doi:[10.1029/2011JD016847](https://doi.org/10.1029/2011JD016847).
- Wu, Z., 2003: A shallow CISK, deep equilibrium mechanism for the interaction between large-scale convection and large-scale circulations in the tropics. *J. Atmos. Sci.*, **60**, 377–392, doi:[10.1175/1520-0469\(2003\)060<0377:ASCDEM>2.0.CO;2](https://doi.org/10.1175/1520-0469(2003)060<0377:ASCDEM>2.0.CO;2).
- Zeng, N., J. D. Neelin, K.-M. Lau, and C. J. Tucker, 1999: Enhancement of interdecadal climate variability in the Sahel by vegetation interaction. *Science*, **286**, 1537–1540, doi:[10.1126/science.286.5444.1537](https://doi.org/10.1126/science.286.5444.1537).
- Zhang, G. J., 1994: Effects of cumulus convection on the simulated monsoon circulation in a general circulation model. *Mon. Wea. Rev.*, **122**, 2022–2038, doi:[10.1175/1520-0493\(1994\)122<2022:E0CCOT>2.0.CO;2](https://doi.org/10.1175/1520-0493(1994)122<2022:E0CCOT>2.0.CO;2).
- Zhang, R., and T. L. Delworth, 2006: Impact of Atlantic multidecadal oscillations on India/Sahel rainfall and Atlantic hurricanes. *Geophys. Res. Lett.*, **33**, L17712, doi:[10.1029/2006GL026267](https://doi.org/10.1029/2006GL026267).
- Zhao, M., 2014: An investigation of the connections among convection, clouds, and climate sensitivity in a global climate model. *J. Climate*, **27**, 1845–1862, doi:[10.1175/JCLI-D-13-00145.1](https://doi.org/10.1175/JCLI-D-13-00145.1).
- , I. M. Held, S.-J. Lin, and G. A. Vecchi, 2009: Simulations of global hurricane climatology, interannual variability, and response to global warming using a 50-km resolution GCM. *J. Climate*, **22**, 6653–6678, doi:[10.1175/2009JCLI3049.1](https://doi.org/10.1175/2009JCLI3049.1).